JGR Space Physics

RESEARCH ARTICLE
10.1029/2024JA032710

Influence of the October 14, 2023, Ring of Fire Annular Eclipse on the Ionosphere: A Comparison Between GNSS Observations and SAMI3 Model Prediction

Sayak Ray[1], J. D. Huba[2], Bhaskar Kundu[1], and Shuanggen Jin[3,4]

[1]Department of Earth and Atmospheric Sciences, NIT Rourkela, Rourkela, Odisha, India, [2]Syntek Technologies, Fairfax, VA, USA, [3]Shanghai Astronomical Observatory, CAS, Shanghai, China, [4]School of Surveying and Land Information Engineering, Henan Polytechnic University, Jiaozuo, China

Abstract Celestial phenomena such as solar eclipses disrupt the ionosphere's inherent photochemical, dynamic, and electrodynamic processes and can be viewed as a natural experiment that provides a unique opportunity to study ionospheric perturbations. We investigate the spatiotemporal ionospheric response induced by the 14 October 2023 annular eclipse using ground-based Global Navigation Satellite System (GNSS) receivers located over the continental region of North and South America. The largest total electron content (TEC) change (~22 TECU decrease) is observed over the path of the eclipse at around 16°–18°N which lies just before the greatest eclipse location. However, the percentage change in TEC here is ~44% (of the background value), which is less than that observed at midlatitudes around 30°–35°N (~18.7 TECU, ~50%). We observed a latitudinal dependency of TEC variation and time delay in ionospheric response to the eclipse with midlatitudes experiencing greater TEC changes and longer time delays compared to low-latitude and equatorial regions. The SAMI3 model used to simulate the impact of the eclipse, captures the large decrease in VTEC along the eclipse path. Interestingly, increases in the TEC are also observed in several GNSS sites and it varied from 4.5 to 6.5 TECU in the Northern Hemisphere and 7 to 12 TECU in the Southern Hemisphere. The SAMI3 model results also show an enhancement in TEC but significantly less than that observed. Moreover, the SAMI3 model simulations for individual GNSS site coordinates within the conjugate regions failed to predict accurately, the TEC enhancement recorded by the GNSS sites.

Key Points:

- The total electron content (TEC) depletion and time delay in ionospheric response to the solar eclipse exhibited a latitudinal dependency within the eclipse region
- SAMI3 model accurately simulated the observed TEC drop in the eclipse region but underpredicted the TEC enhancement in the conjugate regions
- TEC increase in the Southern Hemisphere conjugate region is attributed to uplifted plasma resulting from an enhanced E × B drift velocity

Supporting Information:

Supporting Information may be found in the online version of this article.

Correspondence to:

J. D. Huba and B. Kundu,
jdhuba@gmail.com;
rilbhaskar@gmail.com

Citation:

Ray, S., Huba, J. D., Kundu, B., & Jin, S. (2024). Influence of the October 14, 2023, ring of fire annular eclipse on the ionosphere: A comparison between GNSS observations and SAMI3 model prediction. *Journal of Geophysical Research: Space Physics*, *129*, e2024JA032710. https://doi.org/10.1029/2024JA032710

Received 3 APR 2024
Accepted 10 SEP 2024

Author Contributions:

Conceptualization: Sayak Ray, J. D. Huba, Bhaskar Kundu
Data curation: Sayak Ray
Formal analysis: Sayak Ray, J. D. Huba, Bhaskar Kundu
Funding acquisition: Shuanggen Jin
Investigation: Sayak Ray, J. D. Huba
Methodology: Sayak Ray, J. D. Huba, Bhaskar Kundu
Software: J. D. Huba
Supervision: J. D. Huba, Bhaskar Kundu
Validation: Sayak Ray, Bhaskar Kundu, Shuanggen Jin
Visualization: Sayak Ray, Bhaskar Kundu, Shuanggen Jin
Writing – original draft: Sayak Ray
Writing – review & editing: Sayak Ray, J. D. Huba, Bhaskar Kundu, Shuanggen Jin

1. Introduction

The Earth's space environment has the highest plasma density in the ionosphere (Immel et al., 2006), the ionized portion of the upper atmosphere that encircles the Earth. The major plasma source in this region (between ~80 to about 600 km) is a coupled photoionization (Schunk & Nagy, 2009) and dissociative recombination processes (Strahler, 1963) dominantly via solar radiation flux at EUV (solar extreme ultraviolet) and X-ray wavelengths (https://www.swpc.noaa.gov/) that excites, dissociates, and ionizes neutral molecules and atoms to generate free electron-ion pairs. Ionospheric plasma values are quantified by electron density, which is calculated as the number of electrons in a vertical column per square meter area of cross-section. This quantity is referred to as the Total Electron Content (TEC) (Klobucher, 1991) defined by TECU (where $1\text{TECU} = 1 \times 10^{16}$ electrons/m^2). The TEC is directly linked to the influence of the ionosphere on communication, satellite tracking and navigation applications (Bagiya et al., 2009).

Electron density can be perturbed by a diverse set of natural phenomena such as earthquakes (Cahyadi & Heki, 2015; Catherine et al., 2015, 2016), magnetic storms (Gonzalez et al., 1994), volcanic eruptions (Dautermann et al., 2009; Nakashima et al., 2015) and space shuttle launches (Bowling et al., 2013; Ozeki & Heki, 2010), which can trigger the TEC disturbances by atmospheric waves that propagate into the thermosphere. Solar eclipses (Coster et al., 2017; He et al., 2018; Kundu et al., 2018; Vyas & Sunda, 2012) on the other hand do the same by decreasing the degree of ionisation in the upper ionosphere. Solar eclipses, transiently shield the ionizing solar irradiance (EUV and soft x-rays) in addition to blocking the visible solar radiation. This occultation of the Sun by the Moon can extend over thousands of kilometres, decreasing solar energy input, and thereby causing spatio-temporal changes. The following should be attributed to the general patterns of ionospheric solar eclipse effects: decrease in electron density, change in the rates of chemical reactions, decrease in the temperature of electrons and ions, disturbance of the ionosphere–plasmasphere coupling, the appearance of dynamic processes, generation of travelling ionospheric disturbances (TIDs) and other effects. Across different heights, the ionosphere is influenced

by photochemical reactions occurring below the F2 layer, and transport mechanisms at the F2 layer and higher altitudes (Jakowski et al., 2008; Le, Liu, Yue, Wan, et al., 2009). The effects of solar eclipses on the ionosphere have been comprehensively characterized using several techniques/tools including ground-based ionosonde networks (Evans, 1965; Jakowski et al., 2008; Salah et al., 1986), incoherent scatter radars (ISRs; Baron & Hunsucker, 1973; MacPherson et al., 2000; Goncharenko et al., 2018), Doppler Sounding (Chernogor, 2012; Guo et al., 2020) and complemented by theoretical simulations (e.g., Boitman et al., 1999; Dang et al., 2018; Huba & Drob, 2017; Le et al., 2008a, 2008b, 2010; Le, Liu, Yue, Wan, & Ning, 2009; Lei et al., 2018; Liu et al., 2000; Müller-Wodarg et al., 1998).

Recent developments and continuous worldwide expansion of Global Navigation Satellite Systems (GNSS), which are often used for crustal deformation studies, have also provided researchers with a readily available data source and robust technique to study the dynamics of Earth-ionosphere coupling processes (Catherine et al., 2016; He et al., 2018; Kundu et al., 2018). In fact, in the past decade or so, several studies have focused on the ionospheric responses to solar eclipses such as spatiotemporal depletion in electron density, using GNSS data sets and TEC measurements (Afraimovich et al., 1998, 2002; Cherniak & Zakharenkova, 2018; Coster et al., 2017; Ding et al., 2010; Ding et al., 2010; Tsai & Liu, 1999; Zhang et al., 2017; M. L. Zhang et al., 2021; S. R. Zhang et al., 2021).

Several other papers have been published examining the ionospheric effects of solar eclipses occurring in the past decade such as the 20 March 2015 studied by Chernogor (2016a, 2016b), Chukwuma and Adekoya (2016), Hoque et al. (2016), Stankov et al. (2017), 21 August 2017 studied by Adekoya et al. (2019), Gocharenko et al. (2018), Kundu et al. (2018), Paulino et al. (2020), 11 August 2018 studied by Chernogor and Mylovanov (2020), Guo et al. (2020). Detailed analysis of the three solar eclipses of 2019: 5–6 January (Chernogor, Garmash, Guo, Rozumenko, & Zheng, 2022), 2 July (Jonah et al., 2020) and 26 December (Aa et al., 2020; Barad et al., 2022; Senapati et al., 2020) are provided in these studies. In 2020, the 21 June (Aa et al., 2021; Chernogor, Garmash, Guo, Luo, et al., 2022; Sun et al., 2023) and December 14 (Resende et al., 2021) solar eclipses were analyzed by various methods. The features of the 10 June 2021 solar eclipse are described in Chernogor et al. (2021), Chernogor and Garmash (2022), Chernogor and Mylovanov (2022), Valdés-Abreu et al. (2022). The dynamic effects of 25 October 2022 and 14 October 2023 solar eclipses were also observed (Chauhan et al., 2024; Emelyanov et al., 2024). Despite the extensive research mentioned above, a solar eclipse remains distinctive due to its occurrence in various seasons, at different times of the day, at variable locations, and under different synoptic and geomagnetic conditions (Founda et al., 2007; Kumar & Singh, 2012; Singh et al., 2012). This uniqueness offers another opportunity to compare recent occurrences with past eclipses and review previous conclusions.

During the 14 October 2023, annular eclipse (magnitude 0.952), the Moon's antumbral shadow traversed along a 13,800-km-long track covering 0.57% of the Earth's surface area that extended from the Pacific Ocean (reaching onshore at 9:13 UTC over Oregon, then headed southeast through Nevada and Texas of USA and crossed the Gulf of Mexico and Yucatan Peninsula, leading to Colombia and Brazil in South America) to the Atlantic Ocean (19:48 UTC)—a journey that lasted for more than 3.5 hr (https://earthsky.org/sun/annular-solar-eclipse-october-14-2023/). During this annular solar eclipse, the apparent size of the Moon's disk was 90% (at maximum occultation) of that of the Sun's disk giving rise to a ring of fire around the Moon (https://www.greatamericaneclipse.com/). The closer to this annular path (the curvilinear yellow patch in Figure 1a), the more the sun is eclipsed by the moon.

In this paper, we investigate the spatio-temporal TEC variations in the ionosphere induced by the 2023 October 14 Annular Solar eclipse. Several ground-based GNSS sites over the continental parts of North and South America recorded this event with a significant drop in ionospheric TEC as it impacted the propagation of radio signals. We analyze the quantitative response of the ionosphere/plasmasphere system inside the extent of the eclipse with respect to different latitudes and percentages of obscuration as well as its effect in the geomagnetic conjugate regions. The SAMI3 model is used to simulate the effect of the eclipse event in these regions. We compare the results of GNSS-derived observations with that of the SAMI3 model. Finally, we discuss some of the probable causes of the ionospheric perturbations induced by the eclipse.

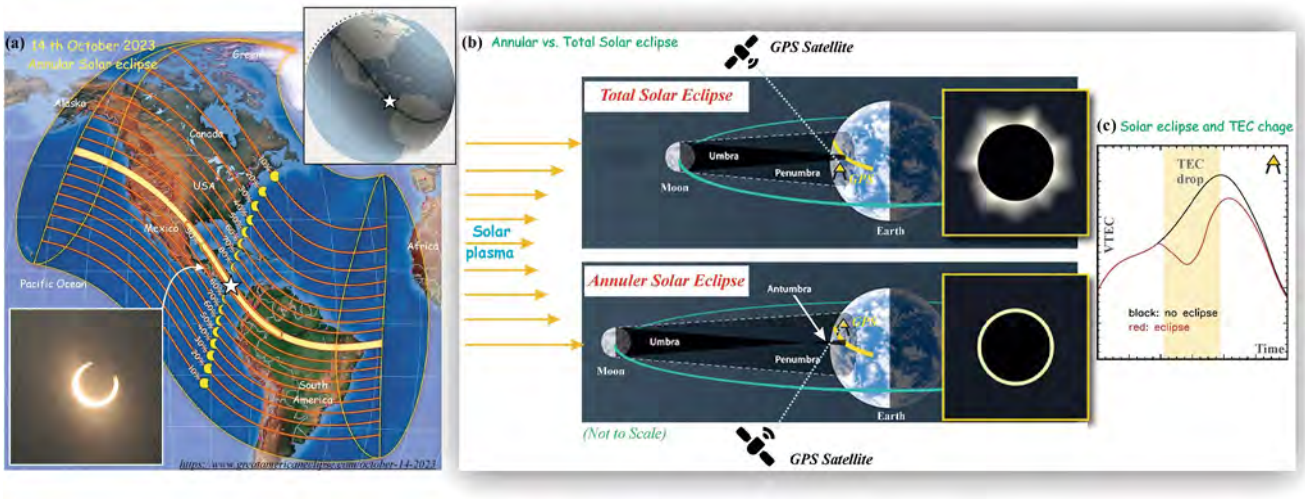

Figure 1. Path, geometry and data acquisition overview of a Solar eclipse: (a) Stereographic view of the 14 October 2023 Annular Solar Eclipse. The path of annularity (highlighted by the light yellow patch) started from the Pacific Ocean and terminated over the Atlantic. The thin yellow lines indicate the fraction (%) of the Sun's diameter covered by the Moon; (Inset) A real-time image of the eclipse as captured by John Dixon from the location indicated by the white arrow. The approximate instant of the greatest eclipse is marked by the white star; (b) Overview of total electron content data recorded by GPS satellites and common geometrical differences in an annular and total solar eclipse is shown with the characteristic images of the sun (halo and ring structure) as viewed from within the umbra and antumbra for a Total and Annular solar eclipse, respectively; (c) A schematic of how a solar eclipse, in general, affects the VTEC in a region with respect to a non-eclipse day.

2. Materials and Methods

2.1. GNSS Data Sets

The daily Receiver INdependent EXchange (RINEX) format data sets (standard sampling rate of 30s) of the permanent GNSS sites located in the region of North and South America were obtained from Scripps Institution of Oceanography's Orbit and Permanent Array Center (SOPAC) (http://sopac-csrc.ucsd.edu/). The daily broadcast ephemeris file (brdc navigation files) for the Eclipse day (Julian Day, 287) and the reference days (Julian Day, 286, 288 and 289) along with some GNSS RINEX data were downloaded from National Oceanic and Atmospheric Administration, NOAA's National Geodetic Survey server (https://geodesy.noaa.gov/corsdata/rinex). The differential code bias (DCB) files (P1C1 and P1P2) for the eclipse day and reference days were accessed from the Center for Orbit Determination in Europe (CODE), Astronomical Institute, University of Bern (http://ftp.aiub.unibe.ch/CODE/). Numerous (>150) sites were processed along the path of the annular eclipse and across, extending northwest away from this path in North America and some available GNSS sites on the conjugate regions of the eclipse were also analyzed.

2.2. Space Weather Data

Disruptive space weather phenomena, such as geomagnetic storms, solar flares and changes in the solar wind which affect the ionospheric electron density and consequently add to the TEC variations, must be at a minimum to be able to truly quantify the effects of an eclipse (or any other transient events as such, natural or anthropogenic) on the ionosphere. We used the Disturbance storm time variation index (Dst) which results from the magnetic disturbance generated by ring current and the three-hour planetary index, Kp to evaluate the Geomagnetic activity, while the solar activity, parameterized in terms of the solar radio flux at 10.7 cm (2,800 MHz) (F10.7 index reported in solar flux unit) was monitored during the eclipse day and a couple of days on either side of the eclipse day (i.e., from 12 Oct to 16 Oct). The above data sets are archived at NASA/GSFC's Space Physics Data Facility's OmniWeb service (https://omniweb.gsfc.nasa.gov/form/dx4.html). Magnetic activity indices describe variations in the geomagnetic field triggered by sudden irregular current systems. The eclipse day fortunately fell under a geomagnetically quiet environment as indicated by the following parameters: Kp $< 4+$, Dst < -30 and F10.7A < 150 (detailed in Figure S1 and Table S1 in Supporting Information S1).

2.3. Data Pertaining to the Eclipse

The data for the spatial coverage of the 14 October 2023, Annular Eclipse is available in. shapefiles and. kml format and was accessed from NASA's Scientific Studio Visualization website (https://svs.gsfc.nasa.gov/5073). Additional information regarding the path of the Moon's antumbral shadow (like the location of northern and southern limits, central line and instant of the Greatest eclipse) was referred from NASA's website (https://eclipse.gsfc.nasa.gov/SEpath/SEpath2001/SE2023Oct14Apath.html).

2.4. GNSS-TEC Data Processing Strategy

The GPS (Global Positioning System) constellations located ∼20,000 km above the Earth's surface, transmit signals on two frequencies (f_1 = 1.5 GHz and f_2 = 1.2 GHz) consisting of two codes P1 (or C/A) and P2. Dual frequency measurements from GPS sites computed by the differential code and the carrier phases yield essential information about the ionosphere. The detailed standard procedure for computing the ionospheric TEC has also been previously discussed (Afraimovich et al., 2001; Calais & Minster, 1995; Carrano & Groves, 2009; Catherine et al., 2016; Heki & Ping, 2005; Panda & Gedam, 2013; Seemala & Valladares, 2011). Broadcast navigation files, receiver and satellite differential code biases, differential phase advance and group delay measurements of the f_1 and f_2 frequencies were used to calculate the Slant TEC (STEC). The dispersive behavior of the ionosphere has a comparable, albeit opposite sign, effect on the code and phase measurements. The TEC is determined at the site using continuous GPS (cGPS) data based on these characteristics as discussed by Komjathy (1997). The corrected STEC measurement is the sum of observed STEC, differential delay of the GPS satellite (satellite bias, b_s) and the receiver (receiver bias, b_R). Similarly, the STEC are then converted to absolute vertical TEC (VTEC) at the ionospheric piercing point (IPP) by the formula (Klobuchar, 1996)

$$VTEC = \frac{[STEC - (b_R + b_S)]}{S(E)} \quad (1)$$

where E is the elevation angle of the satellite (in degrees) and S(E) is the obliquity factor (or the mapping function) for the zenith angle z at IPP (Fedrizzi et al., 2002; Mannucci et al., 1993). The TEC measured using the aforementioned procedure of combining pseudo-range and differential carrier phases contributes to increased accuracy such that absolute TEC cannot be obtained without pseudo-range but it might incur significant noise level to results and the relative TEC variation is precisely provided by the differential carrier phase since the original number of cycles of phase is unknown. Since in the present study, we are solely interested in the variation in TEC during the time of the annular eclipse, the satellite and the receiver biases are of less importance while computing the same. The software used to calculate the STEC and VTEC values from the raw RINEX data was developed by Gopi Seemala and can be openly accessed from http://seemala.blogspot.com/. The variations in TEC are mostly observed in the F2 layer of the ionosphere around the height of maximum ionization (h_{max}) (Kundu et al., 2018).

The impact of elevation angles on GPS signals is significant, particularly at lower angles. Signals received from low elevation angles travel longer paths through the ionosphere, resulting in increased transmission delays and potential errors in observables like pseudoranges and carrier phases due to multipath and atmospheric effects. At these angles, the signal path intersects a broader section of the ionosphere, causing the slant TEC to reach values up to three times greater than at the zenith. Therefore, accurate calculation of the ionospheric TEC is crucial for minimizing errors in GPS positioning. Typically, a 15° elevation mask is applied in GPS surveying to mitigate these effects (Panda & Gedam, 2012). Here, during the time frame of our analysis, the elevation angles remained greater than 20° to ensure continuous and reliable signal reception, thereby reducing multipath, atmospheric, and attenuation errors.

2.5. SAMI3 Modeling Strategy

SAMI3 is a 3D physics-based model of the ionosphere (based on SAMI2 which is a 2D model) (Huba et al., 2000) that simulates the plasma and chemical evolution of seven ion species (H+, He+, N2+, N+, O2+, O+ and NO+). The temperature equation is solved for three ion species (H+, He+ and O+) and the electrons. Ion inertia is included in the ion momentum equation for motion along the geomagnetic field. This is important in modeling the topside ionosphere and plasmasphere where the plasma becomes collisionless. The neutral composition,

temperature, and winds can be specified in SAMI3 by the empirical models NRLMSIS2 (Picone et al., 2002) and HWM14 (Drob et al., 2015). SAMI3 contains 21 chemical reactions and radiative recombination. It uses the EUVAC model for solar radiation. The high latitude electric field is calculated from the empirical Weimer model (2,021) for the potential.

The impact of the 14 October 2023 annular solar eclipse on the ionosphere was predicted or simulated using the SAMI3 model (Huba & Drob, 2017; Huba et al., 2000; Huba & Joyce, 2010). The selected geophysical parameters used in the model for this study are F10.7A ~ 148, Ap = 6 (where F10.7A is the 81-day running mean of solar radio flux at a wavelength of 10.7 cm and Ap is the daily average level for geomagnetic activity) on the Julian day of year 287, corresponding to this eclipse day. SAMI3 uses a non-uniform and non-orthogonal fixed grid for the magnetic latitude range +/− 88°. The neutral wind dynamo-driven electric field is calculated from the solution of a 2D potential equation (Huba et al., 2008).

This grid is based on a dipole field defined as [*nz*, *nf*, *nl*] = [304, 124, 360] where *nz* is the number of cells along a magnetic field line, *nf* is the number of magnetic field lines (~0.2° at low latitude to ~1.5° at high latitude), and *nl* is the longitudinal grid at 1° resolution. The Richmond apex model (Richmond, 1995) is used to specify the geometric magnetic field and geographic conversion factors (i.e., IGRF). The Naval Observatory Vector Astrometry software library (Kaplan et al., 2012), helps to precisely estimate the relative position of the Sun and the Moon. This allows for the computation of obscuration factors, or the percentage of sunlight obstructed, by the event at any given time and location.

The mask used in SAMI3 to obscure the EUV solar radiation is calculated as follows (Huba & Drob, 2017). First, the annular solar eclipse began in the US at time t_i = 16:18 UTC (latitude $\theta_i \sim 44°$N and longitude $\phi_i \sim 124°$W) and ended in the Atlantic Ocean at time t_f = 19:45 UTC (latitude $\theta_f \sim 6.5°$S and longitude $\phi_f \sim 35.7°$W). Across the continents of North and South America, the average velocity is then estimated as $Ve \simeq 0.62$ km s^{-1}. Second, the temporal width of the eclipse to go from full sunlight to maximum obscuration was ~94 min. From this, the radius of obscuration, *Ro* (≃*Ve*to), is estimated to be ~4,000 km. The masked EUV radiation flux is expressed by

$$M(r,t) = \begin{cases} 1 & |r - R_e(t)| \geq R_0 \\ 0.15 + \dfrac{0.75|r - R_e(t)|}{R_0} & |r - R_e(t)| < R_0 \end{cases} \quad (2)$$

where *r* is the position of a SAMI3 grid point projected onto the surface of the Earth and *Re* is the position of the annular solar eclipse on the Earth which can be determined from the latitude $\theta e_{(t)}$ and the longitude $\phi e_{(t)}$ of the annular solar eclipse at time *t*. Equation 5 is based on solar occultation observations and the resulting effective obscuration factors of the 171 Å line as shown in Figure 2 of Huba & Drob, 2017 with a reduced obscuration from 85% to 75%.

3. Results

3.1. Ground-Based GNSS-Derived TEC Observations

We observed the eclipse-influenced changes in ionospheric electron density (quantified by VTEC) over the continental region of North and South America from numerous GNSS sites; observations from the representative ground-based GNSS stations are shown here for presentation purposes. The movement of sub-ionospheric points of PRNs from all cGPS (continuous global positioning system) sites is plotted Figure S2 in Supporting Information S1. For the 8 representative cGPS sites (P034, P070, P040, KSU1, MCTY, LEBA, BAYR and ALGO) extending north-west (white circles in Figure 2a), away the path of the annular eclipse, VTEC time series plot (Figure 2b) shows a systematic decrease in VTEC with increasing percentage of occultation (denoted by blue lines in Figure 2a) of the Sun by the Moon. Here, we refer to the VTEC change as the difference between the peak VTEC prior to the onset of the eclipse and the minimum VTEC value (trough) after the maximum impact of the eclipse on the ionosphere in that region. The maximum VTEC change is obvious at P034 which is located within the path of annularity (i.e., within 90% eclipse intensity). The mean VTEC change of 2 selected PRNs from each site is plotted against the eclipse intensity for the respective region (Figure 2c) and the linear fit (red line in Figure 2c) shows a significant statistical correlation (with $r^2 = 0.91$). The gray-shaded region marks the 95% confidence interval. The primary observable parameters characterizing TEC variations during eclipses include the

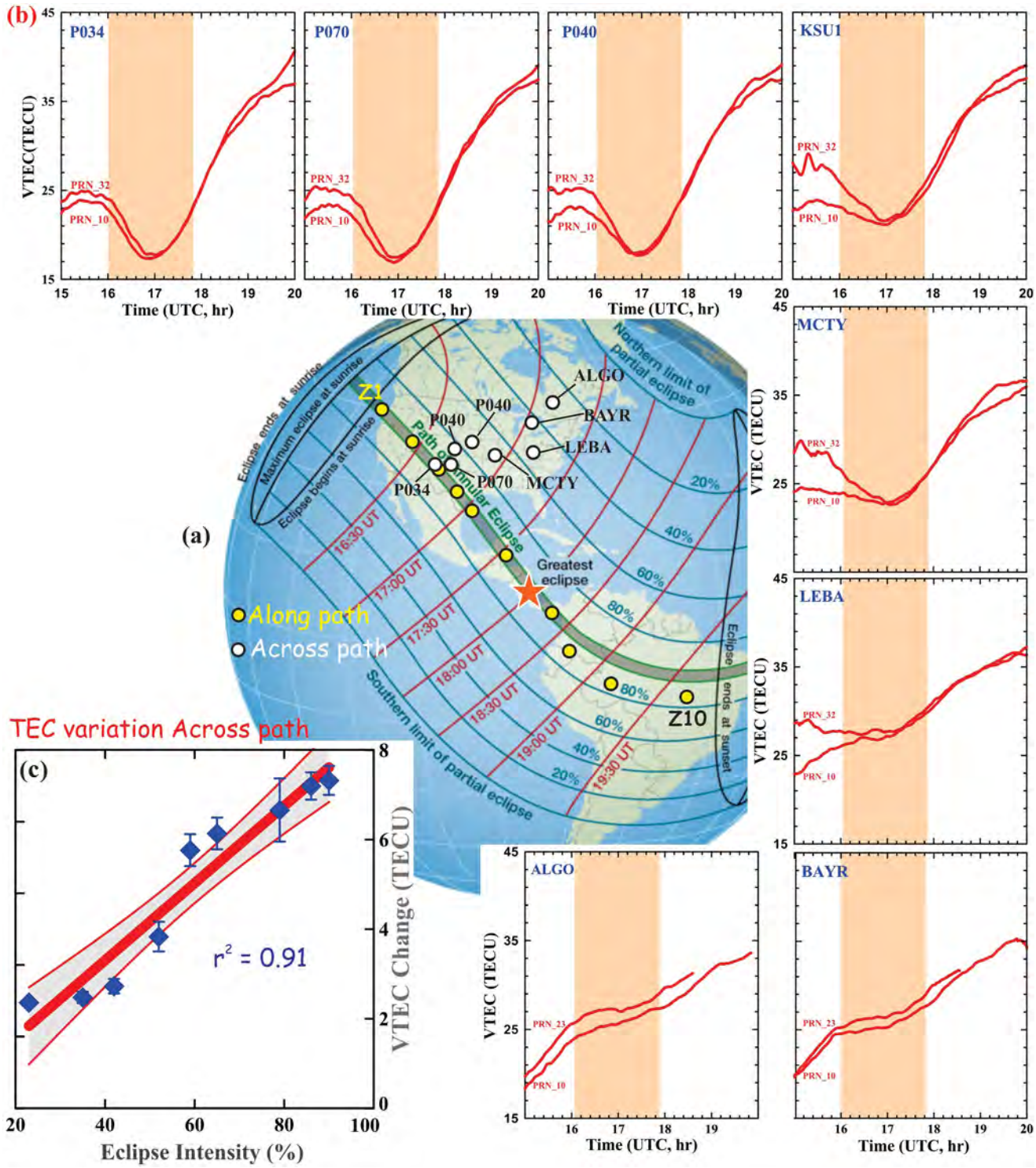

Figure 2.

time delay (t) relative to the maximum phase of the eclipse, the amplitude (A) of TEC change, which is typically characterized by a decrease, and the duration of the perturbation (Afraimovich et al., 2013).

Figure 3 shows the time series VTEC plots during the eclipse day (Julian day 287, in black) with the corresponding reference curves (in red) of 19 representative cGPS sites (P366, P380, FOOT, P080, P034, P120, MDO1, P807, KVTX, CN23, ROA0, GUAT, ACHO, CN55, IBEC, ESMR, CONE, POVE and TOPL) located at (90%) or near (80%–90%) the path of annularity, spread over 10 zones (Zone Z1 to Z10 consisting clusters of GNSS sites). We first compute the average VTEC of the three days, October 13, 15, and 16, 2,024, with solar activity comparable to that of the eclipse day, that is, they fall under geomagnetic calm conditions ($140 < F_{10.7} < 150$; $Dst < -30$ and $K_P < 4+$; Figure S1 and Table S1 in Supporting Information S1). To combine the VTEC of these three reference days we take account of the sidereal day shift (Agnew & Larson, 2007) with respect to the eclipse day. Then we take the mean VTEC of the three reference days for each PRN to generate the reference curves. We added a constant to these reference curves to match them with the pre-eclipse part of the eclipse day VTEC curve. The VTEC change is calculated as the difference between the reference and eclipse day curves where any negative departure from the reference curves is taken as VTEC decrease. A significant depletion in ionospheric TEC over the path of annularity is evident throughout all zones (Z1 TO Z10), however, the magnitude of VTEC change is not uniform. The zonal percentage change in TEC with respect to the background VTEC increased from Z1 (45.5°–41.5°N, 128.5°–118.5°W) and had a peak value of ∼50% at Z3 (37°–34°N, 109°–105°W) and Z4 (32°–29°N, 102°–99°W), thereafter it declined toward the equator. We calculated a maximum of ∼22 TECU drop recorded at the GNSS site CN23 from Z6 (18°–16°N, 89°–86°W consisting of GNSS sites CN23, GUAT and ROA0). This zone also had the highest average VTEC decrease of 20.69 TECU. However, the percentage of TEC with respect to the background was the lowest (∼44%) in this zone among the ones that are located in the mid-latitudes (15°–45°N, Z1–Z6). Aa et al. (2024) conducted a prior investigation of the 14 October 2023, eclipse, utilizing GNSS observations, ionosonde measurements, satellite in situ data, and an innovative TEC-based ionospheric data assimilation system (TIDAS). Their 2D TEC variation results using GNSS data showed a substantial decrease in TEC of 15–25 TECU (25%–45%) over the continental US and Central America. Particularly, within the latitudinal range of 10°–40°N, the average TEC depletion was approximately 13–23 TECU (25%–42%) with the maximum at 13°N. This finding closely aligns with our observations in a comparable range of latitudes (i.e., 8°–44°N), where we noted a TEC depletion of 13–22 TECU (∼24%–50%) and the peak depletion near ∼17°N (CN23). The same study reported a latitudinal dependency such that over the equatorial and low latitude region (10°N–5°S), the TEC reduction of 8–17 TECU (10%–25%) was smaller than at higher latitudes. As per our observations, in the equatorial region (10°–10°S), the VTEC decrease varied from 10 to 14 TECU (15%–25%). For example, the sites in Z7 (9°–7°N, 81°–79°W) situated closest to the region of the greatest eclipse (11°22.2'N, 083°06.1'W over Nicaragua), recorded an average VTEC decrease of 13.35 TECU, similar to that in Z1 (13 TECU) which is at a higher latitude, but the percentage change in VTEC (∼23.6%) in Z7, is significantly lower than in Z1.

We observed that the maximum VTEC change, for all regions over the annular path, occurred after a distinct time delay that is, from the beginning of maximum obscuration till the time of maximum VTEC change over that region (or zone). Such observations were even more prominent for the GNSS sites at midlatitudes (Z1–Z6) located above 15°N. These regions experienced an average time delay of ∼25–40 min which is comparable to the 30–35 min delay observed by Aa et al. (2024) in the mid-latitude region (25°N–45°N). However, in the low latitudes and equatorial regions, we observed significantly shorter time delays (5–22 min) compared to the midlatitudes, consistent with Aa et al. (2024) who reported delays ranging from 5 to 20 min between 5°N and

Figure 2. In focus the total electron content (TEC) variation across the path of annularity: (a) Stereographic view of the 2023 October Annular Solar Eclipse (*Leah Tiscione/Sky and Telescope; source: Fred Espenak* https://skyandtelescope.org/) over which the curvilinear path of annularity (narrow light gray region) which indicates 90% obscuration of the sun by the Moon is highlighted. The majority of this trajectory of the antumbra traverses over the continents of North and South America where the ground-based GNSS stations are located. The yellow circles represent the approximate locations of the 10 clusters (Z1–Z10) of representative GNSS sites used for the computation of TEC change along the path of annularity (note that 3 clusters fall outside the 90% obscuration due to lack of data over the path in those regions). The position of the Greatest eclipse is marked by the orange star. The white circles are of particular importance in this figure as they indicate the specific GNSS sites whose data were used to observe the variation of VTEC (in TECU) at regions that experienced different Eclipse intensity (or the fraction of the Sun's diameter covered by the Moon, denoted by the blue lines) as we move away from the path of annularity; (b) Plot shows temporal variation of VTEC perturbations at 8 representative sites (names of each in blue at top left) with two selected PRNs (representative) located in different eclipse intensity. The light orange bars indicate the timing from pre-eclipse to post-eclipse in the regions selected to compute the change in TEC; (c) The change in VTEC calculated by subtracting the mean of the minimum VTEC values (trough) of 2 PRNs from the mean of pre-eclipse peak VTEC is plotted against the eclipse intensity %.

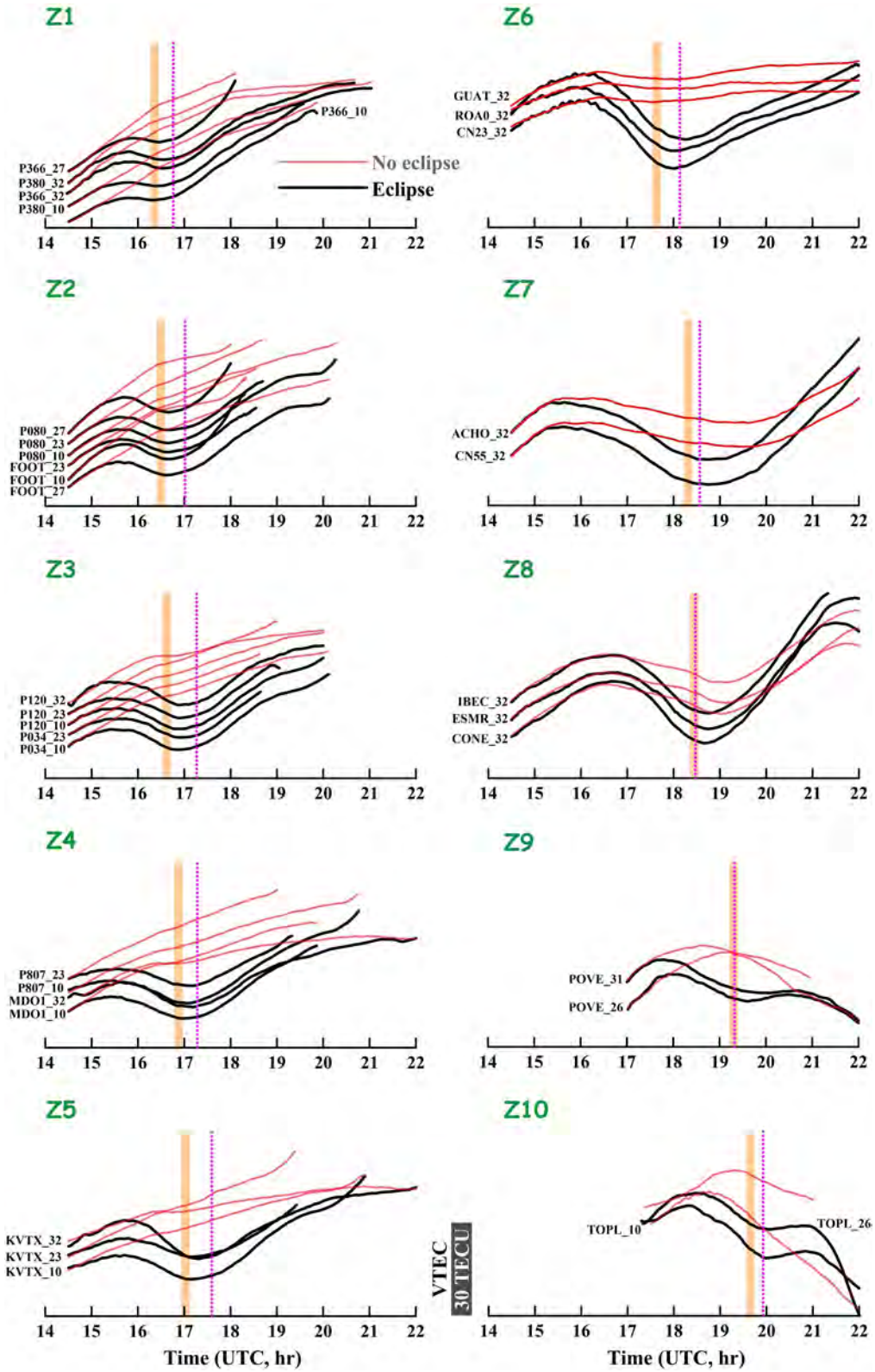

Figure 3.

5°S. Therefore, it is apparent that a smaller TEC depletion corresponds to a shorter time delay and vice versa. The reasons for this latitudinal dependency of ionospheric response have been elaborated in the discussion section. Here, we must acknowledge that due to a lack of data availability over the path of the eclipse, from Z8 to Z10, we selected sites which lie in close proximity (80%–90% obscuration) to the eclipse path to monitor the spatiotemporal variation of the eclipse till its near end over eastern Brazil. The location of each GNSS site is shown in Figure 3 and the corresponding average values recorded are presented Table S3 in Supporting Information S1.

The timings of the eclipse (red lines in Figure 2) over the continental region of North and South America varied as the Moon's antumbra moved from west to east. Consequently, the VTEC minimum recorded by the onshore GNSS satellite data migrated with time (as is evident from the time series in Figure 3) along the path. The travel time (hodochrone) diagram for the TEC depletion during the 14 October 2023 annular eclipse event is shown in Figure 4. The coordinates of the first GNSS station P366 (~43.5°N, 124°W) are taken as a reference for the calculation of the distance of individual PRNs of each of the 19 representative GNSS sites (in Z1–Z10 of Figure 2a). The average hodochrone for the reference days is plotted in Figure 4 (right panel). The timing and location of maximum VTEC depletion for each PRN are plotted over the hodochrone diagram of the eclipse day (Figure 4, left panel). The spatiotemporal fluctuation in TEC adequately reflected the average migration velocity of shadow along the path of the solar eclipse. The slope of the linear fit over this plot, 0.75 km/s is the average migration velocity of Moon's antumbra along the path of annularity. This migration velocity is similar to the estimated velocity for the 21 August 2017 total eclipse (0.74 km/s, Kundu et al., 2018) over the United States but higher than that calculated earlier (0.62 km/s) for the 26 December 2019 annular eclipse (Senapati et al., 2020). As reported earlier, the 2017 Eclipse triggered bow waves as a consequence of the faster-moving shadow of the Moon (Eisenbeis et al., 2019). Additionally, we calculated the orbital velocity of the Moon to be 1.09 km/s as the sum of the estimated average migration velocity of antumbra ~0.75 km/s and Earth's linear velocity at 43.5°N (~0.34 km/s). In addition to the TEC depletion recorded due to the annular eclipse, we observed an increase in VTEC values at certain locations both inside and outside the total domain of the eclipse in the Northern and Southern Hemisphere, respectively. Such results are discussed in the next section in comparison with the SAMI3 model predictions.

3.2. SAMI3 Modeling Results and Comparison With GNSS-Derived Observations

Two SAMI3 model simulations were performed: one for the 14th October eclipse event and another during the same time frame on a non-eclipse day (13 October). The VTEC change (ΔTEC) forecasted by this model is defined as VTEC = TEC (eclipse day)—TEC (non-eclipse day). Figure 5 depicts the spatio-temporal variation of ionospheric electron content as predicted by the SAMI3 model during the 14 October 2023 annular eclipse from 16:30 UTC to 22:00 UTC. The VTEC change (ΔTEC) forecasted by this model over the spatial extent of the eclipse is ~1–20 TECU, with the maximum depletion in VTEC evident around the region of greatest eclipse (Z6 and Z7 in Figures 2 and 3) from Guatemala to Panama and parts of Colombia. Therefore, this model simulated TEC changes are in agreement with our GNSS-derived time series VTEC results (Figure 3 and Movie S1).

Further, the simulated (SAMI3 model predicted) VTEC time series indicates a maximum decrease of ~30–40% relative to the non-eclipse day (Figure 6) for the sites CN23 and ACHO located close to the region of greatest eclipse. This result is in reasonable agreement, both spatially and quantitatively, with the recorded TEC depletion from Z6 and Z7 (containing the two aforementioned GNSS sites) as has been reported in the previous section. However, the simulation results are less consistent for sites (POVE and TOPL) that are located away from the zone of maximum obscuration (90%) or the sites (Figure 6, top panel) located far from the region of greatest eclipse. Additionally, it is apparent from Figure 6, that the ionosphere recovers faster than predicted by the model. One possible reason for the observed discrepancy between the model results and data is that empirical models of the thermosphere are used which may not be representative of the days under study.

Figure 3. Temporal variation of VTEC: total electron content perturbations in the ionosphere were observed in 19 representative onshore GNSS sites located over the path of annularity (except for sites of Zone 8 to 10 which were selected from 80% to 90% obscurity region due to lack of GNSS sites over the 90% path) covering the continents of North and South America during the Eclipse day (Julien Day 287, black curves). The reference curves in light red. The light orange bars cover the duration of maximum obscuration by the eclipse in these regions. The dotted line (magenta) indicates the average time of occurrence of peak depletion in VTEC in that zone. Note that the maximum depletion in VTEC is apparent at sites of Z6 which lies just before the region of greatest eclipse (see Figure 2a).

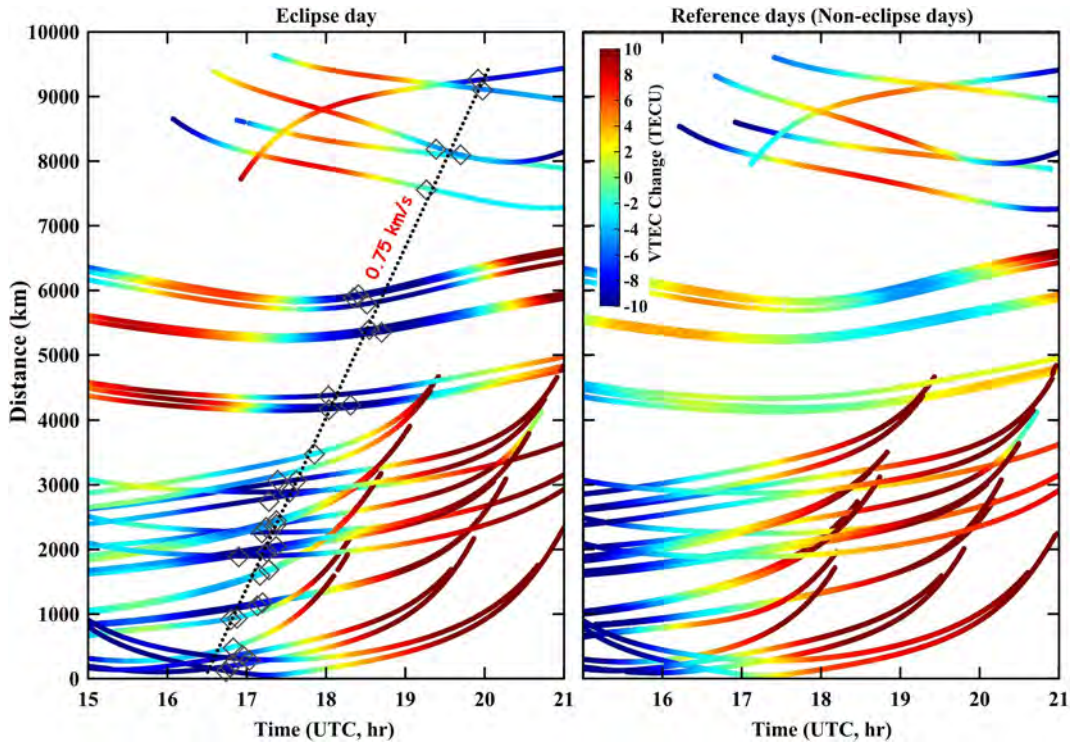

Figure 4. Hodochrone diagram. Ionospheric total electron content depletion during the annular solar eclipse on 14 October 2023 (left panel) and on the reference days (non-eclipse days, right panel). The diamond symbols show the maximum VTEC depletion for individual satellite PRNs. The black dashed line in the left panel indicates the path of the annular solar eclipse. Note that the velocity of the electron depletion during the solar eclipse is about 0.75 km/s.

The SAMI3 model also predicted TEC enhancement in geomagnetic conjugate regions (at large spatial domains) over the eastern coast of Canada and the adjacent Atlantic Ocean in the Northern Hemisphere and parts of Argentina, Chile and the South Atlantic Ocean in the Southern Hemisphere (Figure 7, top panel, and Movie S2). To investigate the same, we analyzed the time series VTEC recorded by GNSS sites in those regions for eclipse (red and blue curves for GNSS sites in the Northern and Southern Hemisphere, respectively) and a non-eclipse day (gray curve). The non-eclipse day curves are taken as a reference. We add a constant to let this reference curve match the pre-eclipse part of the eclipse day curve. Here, we define a positive departure from the reference curve as TEC enhancement and the scaled difference between the two curves at the maxima is termed as an increase in VTEC. This increase in VTEC is greater in the Southern hemisphere (~7–12 TECU, at sites FALK, CORD AND PWRO) than in the Northern hemisphere (~4.5–6.5 TECU, at sites UNBJ, FRDN, BARH, HLFX and SHE2). Such an increase in ionospheric electron density in the geomagnetic conjugate regions is attributed to an enhanced, upward $\vec{E} \times \vec{B}$ drift associated with the eclipse. This is shown in Figure 8 which are contour plots of the differential electron density and $\vec{E} \times \vec{B}$ (eclipse—no eclipse simulation density and drift) at longitude 288° and time 19:35 UT (Figure 8). There is a large relative depletion in the low-to mid-latitude region associated with the eclipse but there is an enhancement in the electron density between −60° and −15° as a function of altitude. This is associated with the uplift of the plasma associated with the upward $\vec{E} \times \vec{B}$ drift velocity shown in the bottom panel of Figure 8. The separatrix between enhancement and depletion is along the F peak layer. This effect is described in Swisdak et al. (2006). Several other hypothesized processes that induce TEC perturbations in the geomagnetic conjugate regions have been summarized in the discussion section.

Since the SAMI3 model does indicate TEC enhancement over a wider region, we wanted to test its robustness to predict this change in TEC at specific GNSS sites. We performed another additional set of simulations for the eclipse and the non-eclipse day at specific GNSS sites or coordinates (BARH, HLFX, SHE2 from the Northern Hemisphere; FALK and PWRO from the Southern Hemisphere) unlike in Figure 7a, where simulations were performed over a large region. The model-predicted VTEC time series plot shows a slight marginal TEC increase

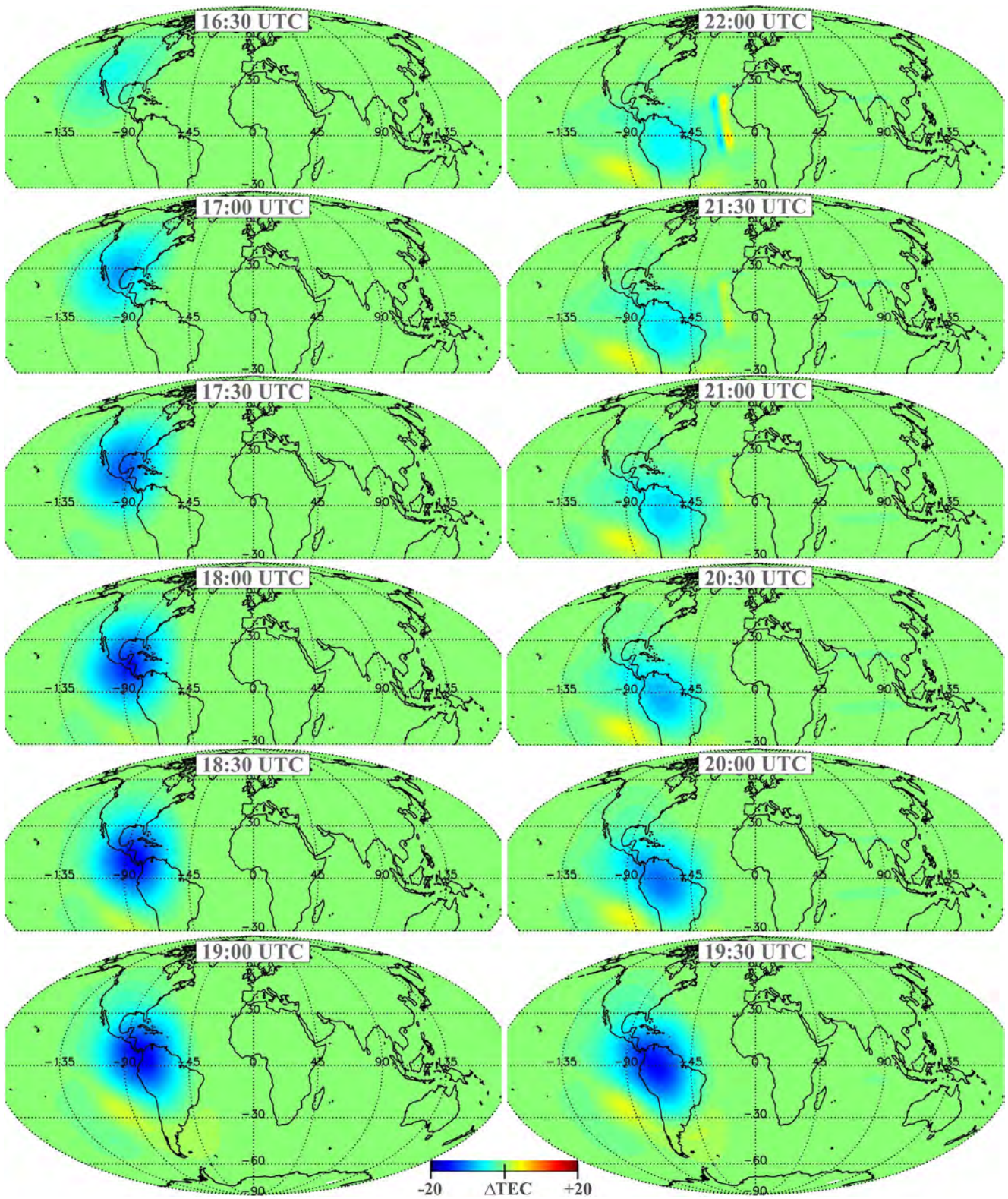

Figure 5. SAMI3 model-predicted spatiotemporal total electron content (TEC) change throughout the duration of the 14 October 2023 annular solar eclipse. The color bar is chosen suitably to highlight the TEC depletion effect observed over the eclipse path from the beginning of the eclipse over Oregon at around ~16:30 UTC till it ended over Brazil at around ~20:00 UTC. The SAMI3 model prediction reveals a further ~2 hr (till 22:00 UTC) till the ionosphere recovers (Captured from the Movie S1).

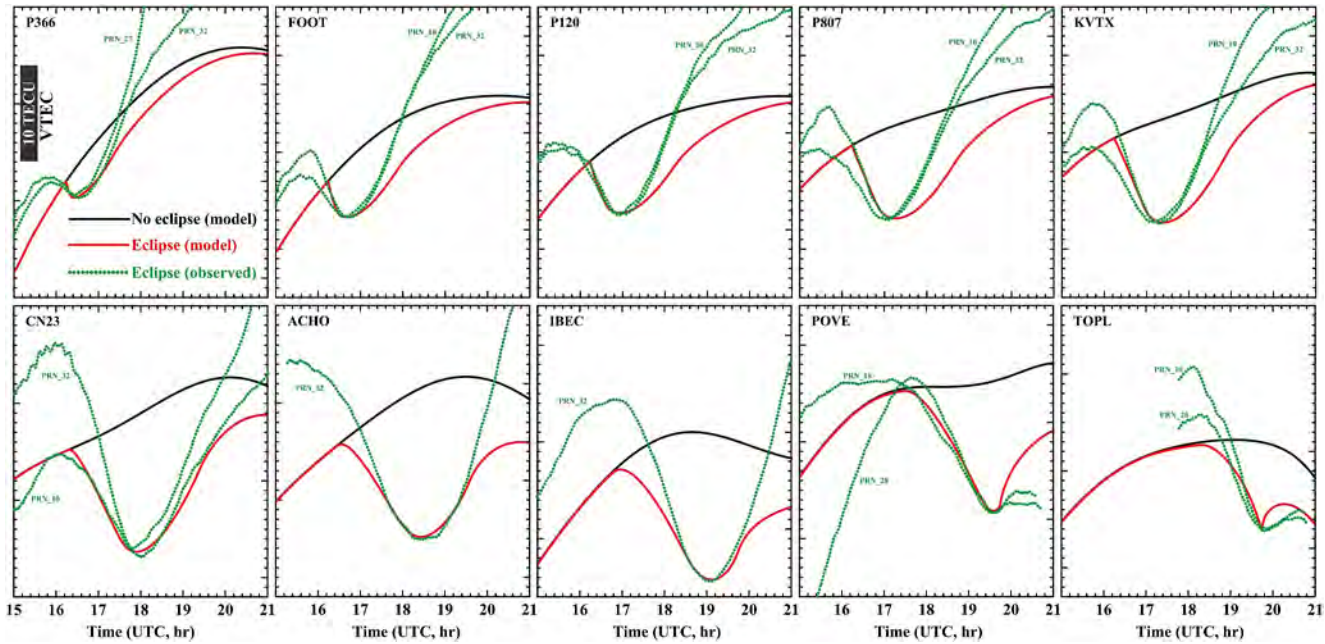

Figure 6. SAMI3 model predicted and GNSS observed total electron content drop time series over the eclipse path: At some of the representative GNSS sites (name in black at the top left corner), the VTEC from model simulations for the eclipse day is shown in red and non-eclipse day in black. Our GNSS-derived VTEC time series for the eclipse day is shown by the green dotted lines.

over two GNSS sites (FALK and PWRO in the southern hemisphere), however, this increment is smaller than what has been captured by the GNSS data (Figure 9). Moreover, the model predictions deviate significantly from the observed GNSS-derived VTEC time series at other individual GNSS sites in the northern hemisphere. Overall the model-predicted TEC increase is not quantitatively consistent with the GNSS-derived VTEC time series plot for the eclipse and non-eclipse day, as is evidenced by a significant deviation of the respective curves and under-prediction in some cases (Figure 9).

4. Discussions

4.1. Comparisons With Other Eclipses

Spectral variability of the solar radiation and the density contrast in the atmosphere facilitates the ionosphere of the Earth to separate into layers, called the *D*, E, and F-layers. Solar irradiance is the dominant cause of ionisation in this layer. At an altitude where the diffusion and chemical time constants are equal, F region density reaches a maximum value (Schunk & Nagy, 2009). The ionosphere, especially the F2 region behaves in a complicated manner and undergoes multiple phases of TEC fluctuations during solar eclipses because of ionisation, diffusion, recombination, temperature changes, conduction and transport (Le, Liu, Yue, Wan, et al., 2009). The eclipse path of the 13 October 2005, annular eclipse (magnitude 0.958) occurred within a similar latitudinal domain (comparatively from high to low latitudes) as the 14 October 2023 eclipse (0.952). The observed TEC reduction was significant, reaching ∼30% depletion within the shadow region. It was assumed that besides eclipse geometry, thermospheric winds contributed to the latitude-dependent depletion pattern (Jakowski et al., 2008). This observation is that TEC change is significantly smaller than the peak depletion (∼50%) observed for the 14 October 2023 eclipse. Chen et al. (2019) used a thermosphere-ionosphere model to study the ionospheric responses of the 21 August 2017 solar eclipse whose path of totality traversed over the mid-latitudes. Their data assimilative analysis of the ionosphere responses indicated a TEC depletion of (∼4 TECU) around 40% with respect to the background TEC near the region of maximum obscuration. For the same eclipse, He et al. (2018) reported a slightly higher VTEC drop of 5–6 TECU which was 40%–50% with respect to the background VTEC. Huba and Drob (2017) using SAMI3 modeling predicted a depletion of electron density ∼50% and a VTEC drop of ∼35% for the 21 August 2017 solar eclipse.

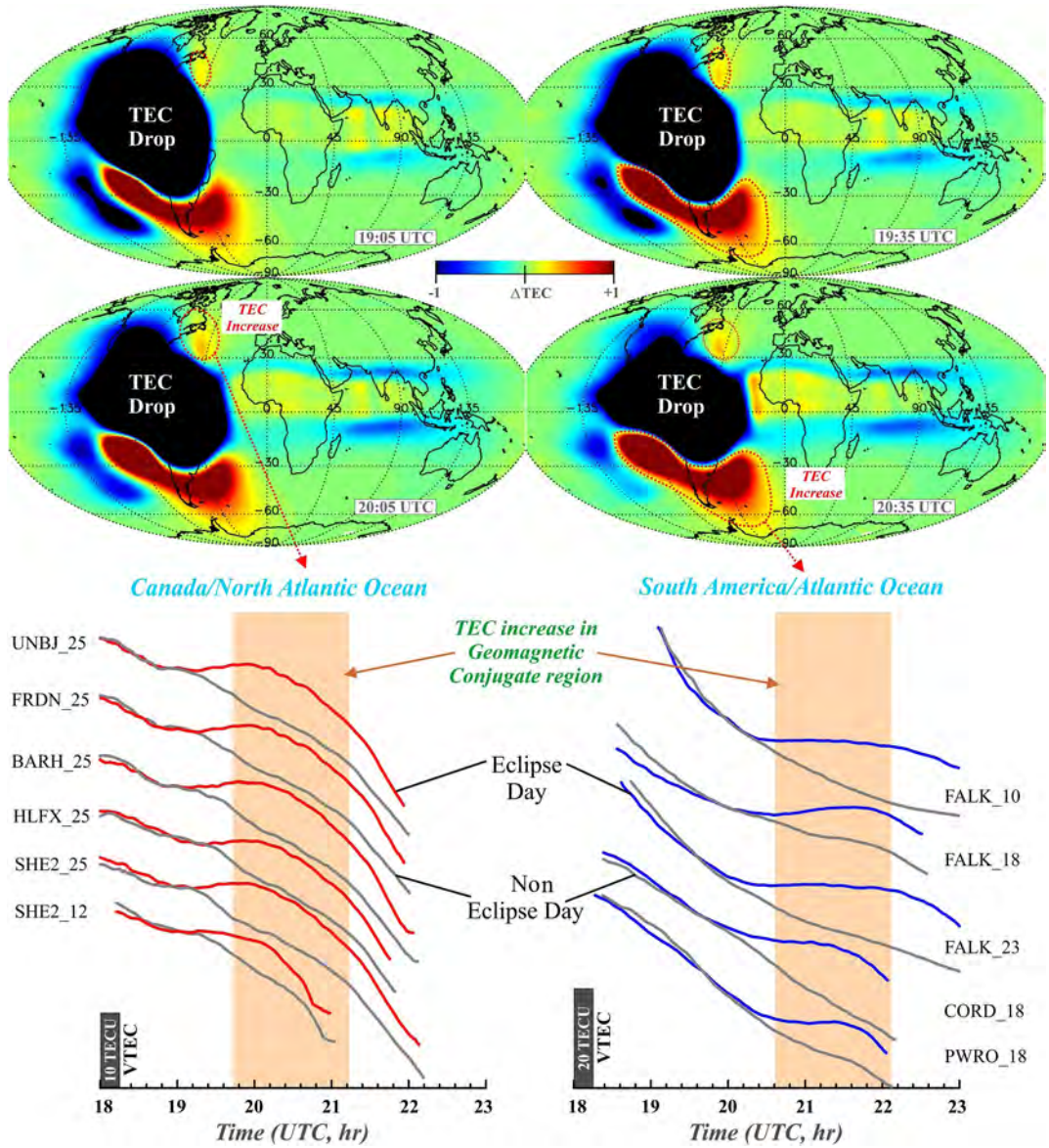

Figure 7. Snapshots of SAMI3 model predicted total electron content (TEC) change from Movie S2 and observed TEC time series for the Conjugate regions: SAMI3 model prediction (top panel) shows the simulated TEC variation with depletion in TEC over the spatial extent of the eclipse covering the Pacific Ocean in the west to the Atlantic Ocean in the east, along with a TEC increase over the northeast coast of Canada and the adjacent Atlantic Ocean in the northern hemisphere and parts of Argentina and Chile in the Southern Hemisphere. Observations from GNSS sites (bottom panel) from these regions indicate a greater increase in VTEC over South America/Atlantic Ocean region (gray: non-eclipse day; blue: eclipse day), than that over Canada/North Atlantic Ocean region (red: eclipse day). The light orange bars delineate a 1.5-hr time span when the above phenomena took place over the respective regions.

Le et al. (2008a) proposed a correlation between local time and a drop in TEC associated with an eclipse such that a larger drop is observed when it occurs around noon-time (10:00–15:00 LT) compared to other local times. This dependency on local time was observed for the 21 June 2020 annular solar eclipse which traversed mostly through the low latitudes (<30°N) and recorded a larger TEC depletion of 5–7 TECU (~40%–50%) during midday and afternoon period (Aa et al., 2021). The 2023 October 14 eclipse, for the greater part of it, over the low latitudes occurred during this noon time and the decrease in VTEC recorded was around 47% (KVTX, Z5). This characteristic aligns with findings from earlier research works (Cherniak & Zakharenkova, 2018; Coster et al., 2017; Ding et al., 2010; Le et al., 2008b). Increased TEC depletion is typically linked to a greater ionospheric loss coefficient due to higher neutral density around midday. Additionally, solar flux at specific altitudes varies with

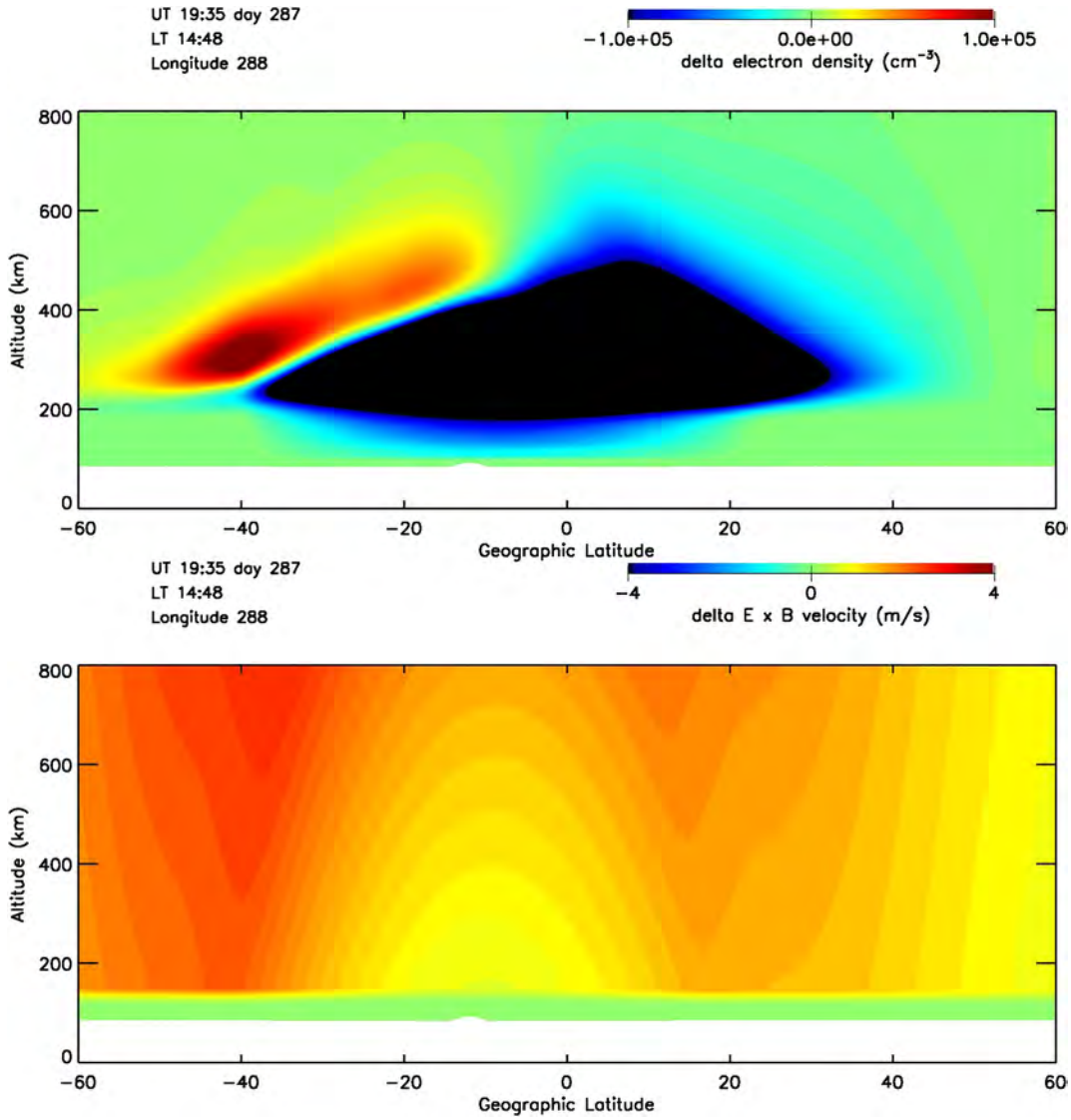

Figure 8. Contour plots of the differential electron density (top panel) and $\vec{E} \times \vec{B}$ drift (bottom 655 panel) (eclipse—no eclipse simulation density and drift) at longitude 288° and time 19:35 UT.

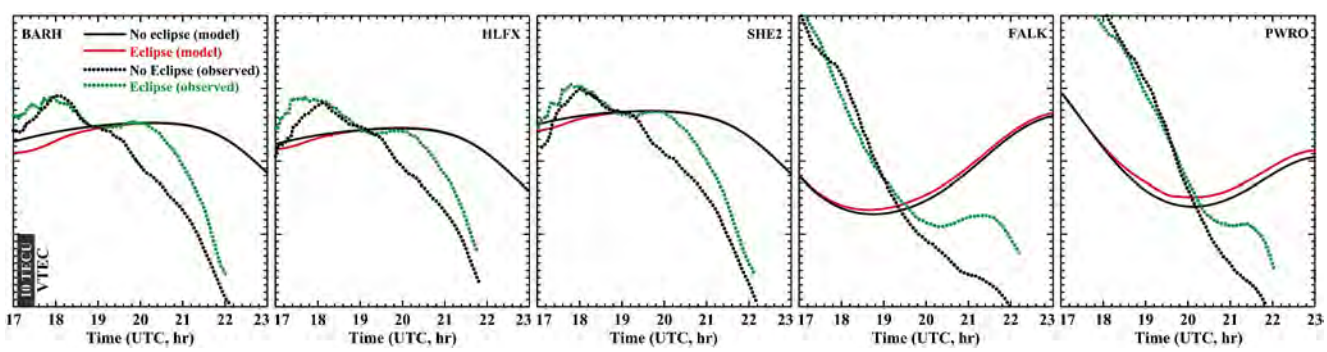

Figure 9. SAMI3 model simulation and observed total electron content (TEC) time series over the conjugate regions: The model simulated VTEC time series (smooth line) at 5 GNSS sites located in the conjugate regions of TEC enhancement for the eclipse day (in red) and non-eclipse day (in black). The dotted lines are the GNSS-derived VTEC plot for the eclipse day (in green) and the non-eclipse day (in black).

the solar zenith angle, which is greater at noon than in the morning. Therefore, a more significant reduction in solar flux during a midday eclipse would also result in a greater absolute TEC depletion. Huang et al., 2020 reported TEC reduction of ∼5 and ∼10 TECU with respect to the reference day at GNSS stations HSKD (29.71°N) and KMNM (24.46°N) located under the maximum obscuration of 89% and 93% respectively. Although the background TEC (∼14–15 TECu) at both stations was quite similar, the eclipse-induced change was double at the later station (KMNM). They attributed this difference to the fountain effect. Huang et al. (1999) used a tomography network for the 24 October 1995 eclipse and observed a TEC enhancement over the low-latitude ionosphere in the Northern Hemisphere. Enhanced foF2 during the 15 January 2010 solar eclipse over Gadanki (13.5°N, 79°E) was reportedly due to weakened electrodynamics that resulted in an equatorward shift of the equatorial ionization anomaly (EIA) crest (Madhav Haridas & Manju, 2012). At high latitudes, ionospheric TEC depletion is affected by space weather effects (Pitout et al., 2013; Rashid et al., 2006) and strong coupling with the magnetosphere. For the 20 March 2015, total eclipse, Hoque et al. (2016) reported an initial plasma depletion of 50%, but after the removal of negative bias due to a strong geomagnetic storm, this came down to ∼30%. The large depletion zone was at 55–65°N latitude and the higher percentage of TEC reduction is due to the lower background TEC levels at high latitudes (Hoque et al., 2016).

The observed ionospheric electron depletion in the 2017 (Kundu et al., 2018) and 2019 eclipses is similar and is of the order of ∼6–8 TECU which is significantly less than our VTEC depletion that ranged from 10 to 22 TECU. We understand that this large variation in VTEC depletion is due to the larger latitudinal coverage (∼44°N to 5°S) of this annular eclipse. In both events, a time-delayed drop in VTEC has been observed. The 26 December 2019 annular eclipse had a maximum TEC depletion of 30%–40% (Senapati et al., 2020) which is the similar to what we have observed in the present case. The time delay for the maximum VTEC depletion for this October 2023 annular eclipse was consistent with a previous study on the same eclipse (Aa et al., 2024; as mentioned in the results section above). According to several sources, during a total eclipse at mid-latitudes, the decrease in TEC generally falls within the range of 30%–40%, with a delay ranging from 20 to 40 min (e.g., Jakowski et al., 2001, 2008; Krankowski et al., 2008). Therefore, it can be concluded that the ionospheric response in terms of TEC for various eclipses is comparable, provided the geomagnetic activity, satellite geometry and geospatial coverage do not vary significantly.

A solar eclipse, although a local phenomenon, when viewed from a regional or even global perspective, suggests that the effects extend beyond the shadow region of the Moon. Global thermospheric circulation may change as a consequence of thermospheric cooling during the eclipse (Dang et al., 2018). In the case of the 21 August 2017 total solar eclipse, GNSS-derived TEC measurements recorded a marginal increase in TEC of ∼1–1.5 TECU, reported from the conjugate region between the northern tip of Antarctica and southern part of South America (He et al., 2018; Kundu et al., 2018) which was consistent with the observations of SAMI3 model simulations (Huba & Drob, 2017). Previously, for the 2019 December 26 annular solar eclipse, the model simulated marginal TEC increase in the conjugate region (over Japan Islands) was reported to be ∼0.2–0.3TECU (Senapati et al., 2020) which was consistent with the ground-based observations Therefore, it is evident that a Northern Hemisphere eclipse (2017 Total solar eclipse and 2019 Annular solar eclipse) can produce TEC enhancement in geomagnetic conjugate regions in both the southern and northern hemispheres. The uniqueness of the 14 October 2023 annular eclipse lies in the fact that it induced TEC enhancement in both the conjugate hemispheres simultaneously. The 3 October 2005, solar eclipse caused a decrease in electron temperature in the Northern Hemisphere and an increase in foF2 and TEC in the conjugate region of the Southern Hemisphere. The conjugate hemisphere experiences a decrease in photoelectron heating and a depression in incoming photoelectrons from the eclipse region. This leads to a decrease in electron temperature and consequent TEC perturbation in the region (Le, Liu, Yue, Wan, & Ning, 2009). However, we found that the TEC enhancement in the conjugate regions was significantly higher than what has been reported by previous studies. It was greater in the southern hemisphere than in the northern hemisphere.

4.2. Summary of Natural Phenomena During a Non-Eclipse and an Eclipse Day

The E-region dynamo, induced by the interaction between neutral winds (thermospheric winds) and the E-layer, generates an eastward electric field on the daytime side. These electric fields propagate upward along magnetic field lines, causing the plasma to $\vec{E} \times \vec{B}$ drift upward at the magnetic equator, raising the F2 layer peak height; we note that the $\vec{E} \times \vec{B}$ drift acts along the magnetic field and lifts plasma to higher altitudes and latitudes (Figure 8)

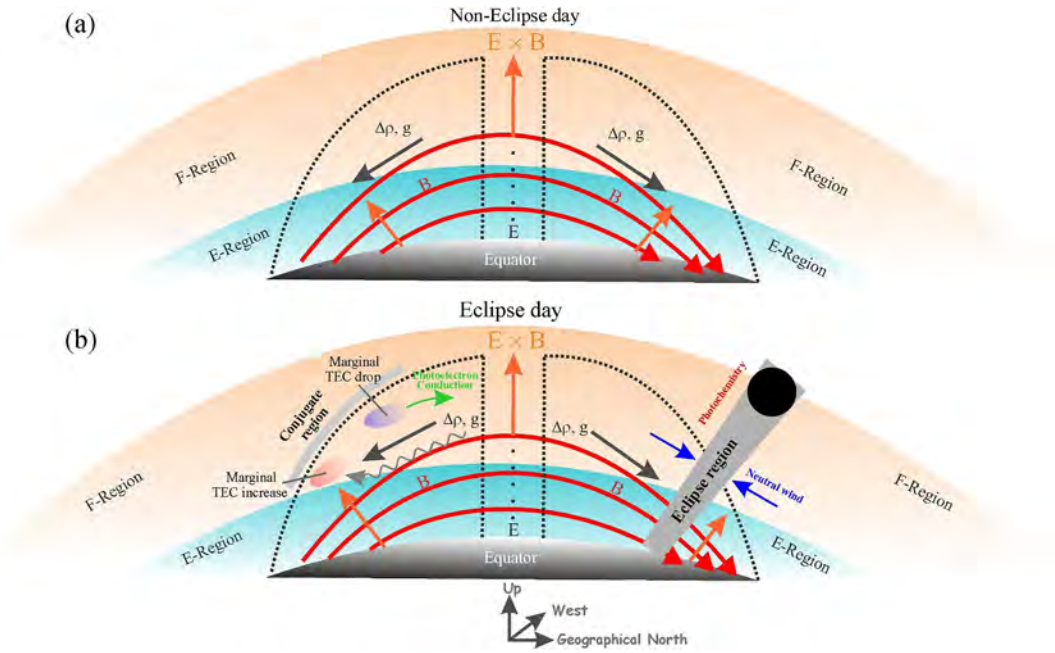

Figure 10. A North-South profile section of the low latitude ionosphere gives a schematic overview of the major phenomena that take place in the region: During (a) In the absence of an eclipse the $\vec{E} \times \vec{B}$ drift is the dominant phenomenon, which raises the plasma that settles down (shown by black arrows) resulting in a fountain effect (shown by black dotted lines) over the subtropical regions on either side of the equator due to differences in density ($\Delta\rho$) and gravitation (g). This gives rise to Appleton anomaly; (b) an eclipse day along with the $\vec{E} \times \vec{B}$ drift, the photochemistry is disturbed by the eclipse, the neutral winds converge and mesoscale ionospheric perturbations are observed both within the eclipse as well as in the conjugate regions (see discussion).

as shown by vectors perpendicular to B (in orange, Figure 10). The combination of diffusion processes and electromagnetic drift results in a fountain effect (Figure 10a) due to the Earth's intrinsic dipolar magnetic field at the ionospheric altitudes (Schunk & Nagy, 2009). Subsequently, the lifted plasma diffuses and gravitationally settles along magnetic field lines, redistributing over the subtropics (±∼15° latitude) on either side of the magnetic equator (Immel et al., 2006) giving rise to ionisation peaks known as the Appleton anomaly or EIA. Figure 10b provides a synopsis of how a solar eclipse affects the ionosphere in multiple ways. Generally, at the start of a solar eclipse, the reduction in EUV radiation causes a decline in photo-chemical and thermodynamic reactions. This results in a gradual reduction in ionospheric plasma density (Afraimovich et al., 1998). Simultaneously, the lunar shadow causes the neutral atmosphere to contract and temperatures to decrease. This alters neutral components like O/N_2 (Reinisch et al., 2018; Wu et al., 2018), and neutral winds converge toward the eclipse center where thermospheric cooling and compositional change take place (e.g., Cnossen et al., 2019; Müller-Wodarg et al., 1998; Wang et al., 2019) (Figure 9b). This phenomenon modifies the $\vec{E} \times \vec{B}$ drift process (Le et al., 2020). Throughout the eclipse, the downward diffusion of plasma from the plasmasphere mitigates the decrease in plasma within the ionospheric F2 region. Specifically, at low latitudes, the electrodynamical processes play a crucial role in the ionospheric response to a solar eclipse (Adeniyi et al., 2007; Cheng et al., 1992; Sridharan et al., 2002; Tsai & Liu, 1999). The substantial decrease in electrons at lower altitudes can propagate to higher altitudes via vertical plasma drift. Additionally, the significant reduction in electron concentration at the equatorial region diminishes the plasma diffusion flux reaching the EIA region along magnetic field lines, thereby influencing how the ionosphere in the EIA region responds to the eclipse (Le, Liu, Yue, Wan, & Ning, 2009).

The ionospheric plasma at the mid-latitudes, is not considerably impacted by magnetospheric electric fields and tends to co-rotate with the Earth. The behavior of ionospheric plasma at midlatitudes is primarily influenced by photochemical reactions and diffusion mechanisms (Aa et al., 2024; Davies, 1990; Rishbeth & Garriott, 1969) but can also be impacted by electrodynamic processes as at lower latitudes (Fejer et al., 1999). Moreover, at mid-latitudes, the dip angle significantly influences how the ionosphere responds during a solar eclipse. A greater dip results in a larger downward diffusion flux, helping to offset plasma loss and lessen the decline in electron density

in the F region. Consequently, at middle latitudes, the responses of NmF2 and TEC to a solar eclipse decrease as latitude increases (Le, Liu, Yue, Wan, & Ning, 2009). Additionally, in the context of a solar eclipse occurring at mid-latitudes, the swift reduction in electron temperature alters the diffusive equilibrium-scale height, causing ionizations to descend from the plasmasphere. This downward movement of ionization serves to counterbalance electron depletion occurring at lower altitudes.

Recent research indicates that the impacts of a solar eclipse on the ionosphere extend beyond local regions, affecting geographic areas outside the eclipse's umbra and penumbra (Aa et al., 2021; He et al., 2018; Le, Liu, Yue, & Wan, 2009; Lei et al., 2018; M. L. Zhang et al., 2021, S. R. Zhang et al., 2021), for example, in the conjugate regions. Researchers have documented that during solar eclipses, cooling of the local plasma induced by the eclipse may conduct along magnetic field lines to the conjugate hemisphere (Figure 10b), resulting in synchronous electron temperature changes that affect the thermodynamics and electron density (Ne) in that region (Huba & Drob, 2017; Le et al., , 2020). However, other studies have suggested photoelectron flux can transfer from the sunlit ionosphere to the dark eclipse region (Figure 10b), partially compensating for the loss of photoelectrons in that area (Aa et al., 2021; Carlson Jr, 1966; Evans & Gastman, 1970; MacPherson et al., 2000; M. L. Zhang et al., 2021, S. R. Zhang et al., 2021). Moreover, during a solar eclipse, electric fields are generated in the ionosphere as a result of changes to the ionospheric dynamo caused by significant alterations in conductivity and/or neutral wind patterns in the E and F regions. These changes have the potential to propagate into the conjugate ionosphere, provided there is no short-circuiting of conjugate currents in the E region (Chen et al., 2019; Dang et al., 2018; Huba & Drob, 2017). Further, examination of the SAMI3 model results has revealed that the $\vec{E} \times \vec{B}$ drift (Figure 8) velocity was enhanced by up to 5 m/s during the eclipse day (relative to the non-eclipse day) as described earlier. This provides an enhancement in the electron density in the southern conjugate region in the F layer because the plasma is lifted to higher altitudes which increases the TEC (Figure 8). This effect is described in Swisdak et al. (2006). The spatiotemporal ionospheric perturbations associated with this annular solar eclipse can be a result of the combined effect of changes in electrodynamical processes in the midlatitude, low latitudes and equatorial regions. While in the geomagnetic conjugate regions, enhanced $\vec{E} \times \vec{B}$ drift velocity caused plasma upliftment that led to the TEC perturbations.

4.3. Limitations of the SAMI3 Model

SAMI3 has been used to model several eclipses and study Medium Scale Traveling Ionospheric Disturbances (MSTIDs). Here, the model does not include eclipse-induced neutral wind modifications. We note that the SAMI3 model predicted TEC variations over a wider domain more or less accurately, however, when its robustness was tested over individual sites in the conjugate regions (Figure 9), that is at a much higher spatial resolution, the results deviated significantly from the GNSS-derived time series. This disagreement between the simulated and observed results for TEC enhancement in the conjugate regions can be associated with certain limitations of the SAMI3 model at a higher spatial resolution that is, for predictions at particular GNSS sites or locations. Some improvements on SAMI3 modeling to be addressed in future are the use of appropriate geophysical conditions (e.g., F10.7, Kp etc), thermosphere response (GITM/TIEGCM/WACCM-X) and creating a more realistic EUV mask by accounting for variations in spectral bands and geometric components (e.g., altitude, eclipse path). Since the ionosphere extends significantly in the vertical direction, there are differences between the eclipse paths at sea level and various altitudes (Verhulst & Stankov, 2020). For instance, in this paper, SAMI3 used an EUV mask at the ground but Verhulst and Stankov (2020) have pointed out that using a different mask at various altitudes can affect the timing and location of the EUV shadow.

5. Conclusions

Based on the above discussions we have come to the following major conclusions:

1. The 14 October 2023 annular eclipse led to a maximum depletion in VTEC of ∼22 TECU (at CN23) along the path of the eclipse, which was perfectly captured by the GNSS sites (in Z6) located near the region of the greatest eclipse. However, with respect to the background VTEC, the depletion of VTEC was maximum (∼50%) at Z3 and Z4 which were at midlatitudes. The TEC depletion and time delay in ionospheric response to the solar eclipse showed latitudinal dependency. The systematic decrease in VTEC in zones of different obscuration %, across the path of the eclipse showed a good linear correlation. The observed TEC depletion was consistent with the SAMI3 model prediction.

2. Results from the SAMI3 model simulations indicated the presence of magnetically conjugate regions in the northern and southern hemispheres. The TEC enhancement in the large spatial domain is qualitatively consistent with the observed results. The under-prediction of TEC enhancement and overall deviation of the simulated results from the observed data must be a limitation of the SAMI3 model at a higher spatial resolution (i.e., for the individual GNSS sites in the conjugate regions).
3. We propose that TEC enhancement in geomagnetically conjugate regions of the Southern Hemisphere (∼7–12 TECU) can be attributed to uplifted plasma as a result of an enhancement in $\vec{E} \times \vec{B}$ drift velocity compared to the non-eclipse day. The cause of asymmetric enhancement in the geomagnetically conjugate region of the North and Southern hemispheres is beyond the scope of this study and requires further analysis in the future.

Conflict of Interest

The authors declare no conflicts of interest relevant to this study.

Data Availability Statement

This work was entirely based on freely available data from the following web resources: GNSS data and brdc navigation files from SOPAC (http://sopac-csrc.ucsd.edu/) and NOAA's National Geodetic Survey server (https://geodesy.noaa.gov/corsdata/rinex); DCB files (P1C1 and P1P2) from CODE (http://ftp.aiub.unibe.ch/CODE/); Space weather data from NASA/GSFC's Space Physics Data Facility's OmniWeb service https://omniweb.gsfc.nasa.gov/form/dx4.html; information of the eclipse were accessed from NASA's website (https://svs.gsfc.nasa.gov/5073) and (https://eclipse.gsfc.nasa.gov/SEpath/SEpath2001/SE2023Oct14Apath.html). The software used to process the GNSS data is available on the website: https://seemala.blogspot.com/. Additionally, this software, all GNSS RINEX and Space weather data sets used in the present study are available in the following data repository https://doi.org/10.6084/m9.figshare.26325292.

Acknowledgments
This work is financially supported by the National Key Research and Development Program (Grant 2021YFA0716100) to Shuanggen Jin. The research of J.D.H. was supported by NASA Grant 80NSSC23K1322. S.R. is supported by the NITR research fellowship. We are thankful to the editor Dr. Viviane Pierrard and the two anonymous reviewers for their constructive comments, which significantly improved the quality of the manuscript.

References

Aa, E., Coster, A. J., Zhang, S. R., Vierinen, J., Erickson, P. J., Goncharenko, L. P., & Rideout, W. (2024). 2-D total electron content and 3-D ionospheric electron density variations during the 14 October 2023 annular solar eclipse. *Journal of Geophysical Research: Space Physics*, *129*(3), e2024JA032447. https://doi.org/10.1029/2024JA032447

Aa, E., Zhang, S. R., Erickson, P. J., Goncharenko, L. P., Coster, A. J., Jonah, O. F., et al. (2020). Coordinated ground-based and space-borne observations of ionospheric response to the annular solar eclipse on 26 December 2019. *Journal of Geophysical Research: Space Physics*, *125*(11), e2020JA028296. https://doi.org/10.1029/2020JA028296

Aa, E., Zhang, S. R., Shen, H., Liu, S., & Li, J. (2021). Local and conjugate ionospheric total electron content variation during the 21 June 2020 solar eclipse. *Advances in Space Research*, *68*(8), 3435–3454. https://doi.org/10.1016/j.asr.2021.06.015

Adekoya, B. J., Adebesin, B. O., David, T. W., Ikubanni, S. O., Adebiyi, S. J., Bolaji, O. S., & Chukwuma, V. U. (2019). Solar-eclipse-induced perturbations at mid-latitude during the 21 August 2017 event. *Annales Geophysicae*, *37*(2), 171–182. https://doi.org/10.5194/angeo-37-171-2019

Adeniyi, J. O., Radicella, S. M., Adimula, I. A., Willoughby, A. A., Oladipo, O. A., & Olawepo, O. (2007). Signature of the 29 March 2006 eclipse on the ionosphere over an equatorial station. *Journal of Geophysical Research*, *112*(A6). https://doi.org/10.1029/2006JA012197

Afraimovich, E. L., Astafyeva, E. I., Demyanov, V. V., Edemskiy, I. K., Gavrilyuk, N. S., Ishin, A. B., et al. (2013). A review of GPS/GLONASS studies of the ionospheric response to natural and anthropogenic processes and phenomena. *Journal of Space Weather and Space Climate*, *3*, A27. https://doi.org/10.1051/swsc/2013049

Afraimovich, E. L., Kosogorov, E. A., & Lesyuta, O. S. (2001). Ionospheric response to the total solar eclipse of August 11, 1999, as deduced from the data from the European GPS network. *Advances in Space Research*, *27*(6–7), 1351–1354. https://doi.org/10.1016/S0273177(01)00191-0

Afraimovich, E. L., Kosogorov, E. A., & Lesyuta, O. S. (2002). Effects of the August 11, 1999 total solar eclipse as deduced from total electron content measurements at the GPS network. *Journal of Atmospheric and Solar-Terrestrial Physics*, *64*(18), 1933–1941. https://doi.org/10.1016/S1364-6826(02)00221-3

Afraimovich, E. L., Palamartchouk, K. S., Perevalova, N. P., Chernukhov, V. V., Lukhnev, A. V., & Zalutsky, V. T. (1998). Ionospheric effects of the solar eclipse of March 9, 1997, as deduced from GPS data. *Geophysical Research Letters*, *25*(4), 465–468. https://doi.org/10.1029/98GL00186

Agnew, D. C., & Larson, K. M. (2007). Finding the repeat times of the GPS constellation. *GPS Solutions*, *11*(1), 71–76. https://doi.org/10.1007/s10291-006-0038-4

Bagiya, M. S., Joshi, H. P., Iyer, K. N., Aggarwal, M., Ravindran, S., & Pathan, B. M. (2009). TEC variations during low solar activity period (2005–2007) near the equatorial ionospheric anomaly crest region in India. In *Annales geophysicae, annales geophysicae* (Vol. 27(3), pp. 1047–1057). Copernicus GmbH. https://doi.org/10.5194/angeo-27-1047-2009

Barad, R. K., Sripathi, S., & England, S. L. (2022). Multi-instrument observations of the ionospheric response to the 26 December 2019 solar eclipse over Indian and Southeast Asian longitudes. *Journal of Geophysical Research: Space Physics*, *127*(9), e2022JA030330. https://doi.org/10.1029/2022JA030330

Baron, M. J., & Hunsucker, R. D. (1973). Incoherent scatter radar observations of the auroral zone ionosphere during the total solar eclipse of July 10, 1972. *Journal of Geophysical Research*, *78*(31), 7451–7460. https://doi.org/10.1029/JA078i031p07451

Boitman, O. N., Kalikhman, A. D., & Tashchilin, A. V. (1999). The midlatitude ionosphere during the total solar eclipse of March 9, 1997. *Journal of Geophysical Research*, *104*(A12), 28197–28206. https://doi.org/10.1029/1999JA900228

Bowling, T., Calais, E., & Haase, J. S. (2013). Detection and modelling of the ionospheric perturbation caused by a space shuttle launch using a network of ground-based global positioning system stations. *Geophysical Journal International*, *192*(3), 1324–1331. https://doi.org/10.1093/gji/ggs101

Cahyadi, M. N., & Heki, K. (2015). Coseismic ionospheric disturbance of the large strike-slip earthquakes in North Sumatra in 2012: *Mw* dependence of the disturbance amplitudes. *Geophysical Journal International*, *200*(1), 116–129. https://doi.org/10.1093/gji/ggu343

Calais, E., & Minster, J. B. (1995). GPS detection of ionospheric perturbations following the January 17, 1994, Northridge earthquake. *Geophysical Research Letters*, *22*(9), 1045–1048. https://doi.org/10.1029/95GL00168

Carlson, H. C., Jr. (1966). Ionospheric heating by magnetic conjugate-point photoelectrons. *Journal of Geophysical Research*, *71*(1), 195–199. https://doi.org/10.1029/JZ071i001p00195

Carrano, C., & Groves, K. (2009). Ionospheric data processing and analysis, workshop on satellite navigation science and technology for Africa.

Catherine, J. K., Maheshwari, D. U., Gahalaut, V. K., Roy, P. N. S., Khan, P. K., & Puviarasan, N. (2016). Ionospheric disturbances triggered by the 25 April 2015 *M*7.8 Gorkha earthquake, Nepal: Constraints from GPS TEC measurements. *Journal of Asian Earth Sciences*, *133*, 80–88. https://doi.org/10.1016/j.jseaes.2016.07.014

Catherine, J. K., Vijayan, M. S. M., Syeda Rabiya, U. B., Shimna, K., Gahalaut, V. K., & Ramesh, D. S. (2015). Dichotomy in mode propagation of coseismic ionospheric disturbance: Observations from 11 April 2012 Indian Ocean earthquake. *Journal of Geophysical Research: Space Physics*, *120*(5), 3854–3867. https://doi.org/10.1002/2014JA020621

Chauhan, V., Singh, R., Singh, S., Singh, V., & Singh, O. P. (2024). The dynamic effects of solar eclipses of October 25, 2022, and October 14, 2023, on GPS-derived total electron content. *Geodesy and Geodynamics*. https://doi.org/10.1016/j.geog.2024.06.003

Chen, C. H., Lin, C. H. C., & Matsuo, T. (2019). Ionospheric responses to the 21 August 2017 solar eclipse by using data assimilation approach. *Progress in Earth and Planetary Science*, *6*, 1–9. https://doi.org/10.1186/s40645-019-0263-4

Cheng, K., Huang, Y. N., & Chen, S. W. (1992). Ionospheric effects of the solar eclipse of September 23, 1987, around the equatorial anomaly crest region. *Journal of Geophysical Research*, *97*(A1), 103–111. https://doi.org/10.1029/91JA02409

Cherniak, I., & Zakharenkova, I. (2018). Ionospheric total electron content response to the great American solar eclipse of 21 August 2017. *Geophysical Research Letters*, *45*(3), 1199–1208. https://doi.org/10.1002/2017GL075989

Chernogor, L. F. (2012). Effects of solar eclipses in the ionosphere: Results of Doppler sounding: 1. Experimental data. *Geomagnetism and Aeronomy*, *52*(6), 768–778. https://doi.org/10.1134/S0016793212050039

Chernogor, L. F. (2016a). Wave processes in the ionosphere over Europe that accompanied the solar eclipse of March 20, 2015. *Kinematics and Physics of Celestial Bodies*, *32*(4), 196–206. https://doi.org/10.3103/S0884591316040024

Chernogor, L. F. (2016b). Atmosphere–ionosphere response to solar eclipse over Kharkiv on March 20, 2015. *Geomagnetism and Aeronomy*, *56*(5), 592–603. https://doi.org/10.1134/S0016793216050030

Chernogor, L. F., & Garmash, K. P. (2022). Ionospheric processes during the partial solar eclipse above Kharkiv on June 10, 2021. *Kinematics and Physics of Celestial Bodies*, *38*(2), 61–72. https://doi.org/10.3103/S0884591322020039

Chernogor, L. F., Garmash, K. P., Guo, Q., Luo, Y., Rozumenko, V. T., & Zheng, Y. (2022). Some features of the ionospheric radio wave characteristics over China observed during the solar eclipse of 21 June 2020. *Radio Science*, *57*(10), 1–21. https://doi.org/10.1029/2022RS007492

Chernogor, L. F., Garmash, K. P., Guo, Q., Rozumenko, V. T., & Zheng, Y. (2022). Ionospheric effects of the 5–6 january 2019 eclipse over the people's Republic of China: Results from oblique sounding. *Annales Geophysicae*, *40*(5), 585–603. https://doi.org/10.5194/angeo-40-585-2022

Chernogor, L. F., Garmash, K. P., Zhdanko, Y. H., Leus, S. G., & Luo, Y. (2021). Features of ionospheric effects from the partial solar eclipse over the city of Kharkiv on 10 June 2021. *Radio Physics and Radio Astronomy*, *26*(4), 326–343. https://doi.org/10.15407/rpra26.04.326

Chernogor, L. F., & Mylovanov, Y. B. (2020). Ionospheric effects of the August 11, 2018, solar eclipse over the People's Republic of China. *Kinematics and Physics of Celestial Bodies*, *36*(6), 274–290. https://doi.org/10.3103/S0884591320060021

Chernogor, L. F., & Mylovanov, Y. B. (2022). Ionospheric effects of the June 10, 2021, solar eclipse in the Arctic. *Kinematics and Physics of Celestial Bodies*, *38*(4), 197–209. https://doi.org/10.3103/S088459132204002X

Chukwuma, V. U., & Adekoya, B. J. (2016). The effects of March 20 2015 solar eclipse on the F2 layer in the mid-latitude. *Advances in Space Research*, *58*(9), 1720–1731. https://doi.org/10.1016/j.asr.2016.06.038

Cnossen, I., Ridley, A. J., Goncharenko, L. P., & Harding, B. J. (2019). The response of the ionosphere-thermosphere system to the 21 August 2017 solar eclipse. *Journal of Geophysical Research: Space Physics*, *124*(8), 7341–7355. https://doi.org/10.1029/2018JA026402

Coster, A. J., Goncharenko, L., Zhang, S.-R., Erickson, P. J., Rideout, W., & Vierinen, J. (2017). GNSS observations of ionospheric variations during the 21 August 2017 solar eclipse. *Geophysical Research Letters*, *44*(24), 12041–12048. https://doi.org/10.1002/2017GL075774

Dang, T., Lei, J., Wang, W., Zhang, B., Burns, A., Le, H., et al. (2018). Global responses of the coupled thermosphere and ionosphere system to the August 2017 Great American Solar Eclipse. *Journal of Geophysical Research: Space Physics*, *123*(8), 7040–7050. https://doi.org/10.1029/2018JA025566

Dautermann, T., Calais, E., Lognonne, P., & Mattioli, G. S. (2009). Lithosphere–atmosphere–ionosphere coupling after the 2003 explosive eruption of the Soufriere Hills volcano, Montserrat. *Geophysical Journal International*, *179*(3), 1537–1546. https://doi.org/10.1111/j.1365-246X.2009.04390.x

Davies, K. (1990). *Ionospheric radio*. Peter Peregrinus. https://doi.org/10.1049/PBEW031E

Ding, F., Wan, W., Ning, B., Liu, L., Le, H., Xu, G., et al. (2010). GPS TEC response to the 22 July 2009 total solar eclipse in East Asia. *Journal of Geophysical Research*, *115*(A7), A07308. https://doi.org/10.1029/2009JA015113

Drob, D. P., Emmert, J. T., Meriwether, J. W., Makela, J. J., Doornbos, E., Conde, M., et al. (2015). An update to the Horizontal Wind Model (HWM): The quiet time thermosphere. *Earth and Space Science*, *2*(7), 301–319. https://doi.org/10.1002/2014EA000089

Eisenbeis, J., Occhipinti, G., Astafyeva, E., & Rolland, L. (2019). Short-and long-wavelength TIDs generated by the great American eclipse of 21 August 2017. *Journal of Geophysical Research: Space Physics*, *124*(11), 9486–9493. https://doi.org/10.1029/2019JA026919

Emelyanov, L. Y., Bogomaz, O. V., Chernogor, L. F., & Domnin, I. F. (2024). Response of the mid-latitude ionosphere to the solar eclipse on 25 October 2022: Results of F2–layer vertical sounding. *Advances in Space Research*, *73*(5), 2338–2354. https://doi.org/10.1016/j.asr.2023.12.034

Evans, J. V. (1965). On the behavior of f_0 F_2 during solar eclipses. *Journal of Geophysical Research*, *70*(3), 733–738. https://doi.org/10.1029/JZ070I003P00733

Evans, J. V., & Gastman, I. J. (1970). Detection of conjugate photoelectrons at Millstone hill. *Journal of Geophysical Research*, *75*(4), 807–815. https://doi.org/10.1029/JA075i004p00807

Fedrizzi, M., Paula, E., Langley, R., Santos, M., & Komjathy, A. (2002). Mapping the low latitude ionosphere with GPS. *GPS World*, *13*(2), 41–47.

Fejer, B. G., Scherliess, L., & de Paula, E. R. (1999). Effects of the vertical plasma drift velocity on the generation and evolution of equatorial spread F. *Journal of Geophysical Research*, *104*(19), 859–19869. https://doi.org/10.1029/1999ja900271

Founda, D., Melas, D., Lykoudis, S., Lisaridis, I., Gerasopoulos, E., Kouvarakis, G., et al. (2007). The effect of the total solar eclipse of 29 March 2006 on meteorological variables in Greece. *Atmospheric Chemistry and Physics*, *7*(21), 5543–5553. https://doi.org/10.5194/acp-7-5543-2007

Goncharenko, L. P., Erickson, P. J., Zhang, S. R., Galkin, I., Coster, A. J., & Jonah, O. F. (2018). Ionospheric response to the solar eclipse of 21 August 2017 in Millstone Hill (42N) observations. *Geophysical Research Letters*, *45*(10), 4601–4609. https://doi.org/10.1029/2018GL077334

Gonzalez, W. D., Joselyn, J. A., Kamide, Y., Kroehl, H. W., Rostoker, G., Tsurutani, B. T., & Vasyliunas, V. M. (1994). What is a geomagnetic storm? *Journal of Geophysical Research*, *99*(A4), 5771–5792. https://doi.org/10.1029/93JA02867

Guo, Q., Chernogor, L. F., Garmash, K. P., Rozumenko, V. T., & Zheng, Y. (2020). Radio monitoring of dynamic processes in the ionosphere over China during the partial solar eclipse of 11 August 2018. *Radio Science*, *55*(2), e2019RS006866. https://doi.org/10.1029/2019RS006866

He, L., Heki, K., & Wu, L. (2018). Three-dimensional and trans-hemispheric changes in ionospheric electron density caused by the great solar eclipse in North America on 21 August 2017. *Geophysical Research Letters*, *45*(20), 10933–10940. https://doi.org/10.1029/2018gl080365

Heki, K., & Ping, J. (2005). Directivity and apparent velocity of the coseismic ionospheric disturbances observed with a dense GPS array. *Earth and Planetary Science Letters*, *236*(3–4), 845–855. https://doi.org/10.1016/j.epsl.2005.06.010

Hoque, M. M., Wenzel, D., Jakowski, N., Gerzen, T., Berdermann, J., Wilken, V., et al. (2016). Ionospheric response over Europe during the solar eclipse of March 20, 2015. *Journal of Space Weather and Space Climate*, *6*, A36. https://doi.org/10.1051/swsc/2016032

Huang, C. R., Liu, C. H., Yeh, K. C., Lin, K. H., Tsai, W. H., Yeh, H. C., & Liu, J. Y. (1999). A study of tomographically reconstructed ionospheric images during a solar eclipse. *Journal of Geophysical Research*, *104*(A1), 79–94. https://doi.org/10.1029/98JA02531

Huang, F., Li, Q., Shen, X., Xiong, C., Yan, R., Zhang, S. R., et al. (2020). Ionospheric responses at low latitudes to the annular solar eclipse on 21 June 2020. *Journal of Geophysical Research: Space Physics*, *125*(10), e2020JA028483. https://doi.org/10.1029/2020ja028483

Huba, J. D., & Drob, D. (2017). SAMI3 prediction of the impact of the 21 August 2017 total solar eclipse on the ionosphere/plasmasphere system. *Geophysical Research Letters*, *44*(12), 5928–5935. https://doi.org/10.1002/2017GL073549

Huba, J. D., & Joyce, G. (2010). Global modeling of equatorial plasma bubbles. *Geophysical Research Letters*, *37*(17). https://doi.org/10.1029/2010GL044281

Huba, J. D., Joyce, G., & Fedder, J. A. (2000). Sami2 is another model of the ionosphere (SAMI2): A new low-latitude ionosphere model. *Journal of Geophysical Research*, *105*(A10), 23035–23053. https://doi.org/10.1029/2000JA000035

Huba, J. D., Joyce, G., & Krall, J. (2008). Three-dimensional equatorial spread F modelling. *Geophysical Research Letters*, *35*(10). https://doi.org/10.1029/2008GL033509

Immel, T. J., Sagawa, E., England, S. L., Henderson, S. B., Hagan, M. E., Mende, S. B., et al. (2006). Control of equatorial ionospheric morphology by atmospheric tides. *Geophysical Research Letters*, *33*(15). https://doi.org/10.1029/2006GL026161

Jakowski, N., Heise, S., Wehrenpfennig, A., & Schlueter, S. (2001). Total electron content studies of the solar eclipse on 11 August 1999. In *Proceedings*.

Jakowski, N., Stankov, S. M., Wilken, V., Borries, C., Altadill, D., Chum, J., et al. (2008). Ionospheric behavior over Europe during the solareclipse of 3 October 2005. *Journal of Atmospheric and Solar-Terrestrial Physics*, *70*(6), 836–853. https://doi.org/10.1016/j.jastp.2007.02.016

Jonah, O. F., Goncharenko, L., Erickson, P. J., Zhang, S., Coster, A., Chau, J. L., et al. (2020). Anomalous behavior of the equatorial ionization anomaly during the 2 July 2019 solar eclipse. *Journal of Geophysical Research: Space Physics*, *125*(9), e2020JA027909. https://doi.org/10.1029/2020JA027909

Kaplan, G., Bartlett, J. L., Monet, A., Bangert, J., Puatua, W., Harris, W., et al. (2012). NOVAS: Naval observatory vector astrometry software. *Astrophysics Source Code Library*, *1*, 02003.

Klobuchar, J. A. (1991). Ionospheric effects on GPS. *GPS World*, *2*, 48–51.

Klobuchar, J. A. (1996). Ionospheric effects on GPS. In B. W. Parkinson & J. J. Spilker (Eds.), *Global positioning system: Theory and applications* (Vol. 1, pp. 485–515). American Institute of Aeronautics and Astronautics INC.

Komjathy, A. (1997). Global ionospheric total electron content mapping using the global positioning system. In *Ph.D. Dissertation, dept. Of geodesy and geomatics engineering*. University of New Brunswick.

Krankowski, A., Shagimuratov, I. I., Baran, L. W., & Yakimova, G. A. (2008). The effect of total solar eclipse of October 3, 2005, on the total electron content over Europe. *Advances in Space Research*, *41*(4), 628–638. https://doi.org/10.1016/j.asr.2007.11.002

Kumar, S., & Singh, A. K. (2012). Changes in Total Electron Content (TEC) during the annular solar eclipse of 15 January 2010. *Advances in Space Research*, *49*(1), 75–82. https://doi.org/10.1016/j.asr.2011.09.017

Kundu, B., Panda, D., Gahalaut, V. K., & Catherine, J. K. (2018). The August 21, 2017 American total solar eclipse through the eyes of GPS. *Geophysical Journal International*, *214*(1), 651–655. https://doi.org/10.1093/gji/ggy149

Le, H., Liu, L., Ding, F., Ren, Z., Chen, Y., Wan, W., et al. (2010). Observations and modeling of the ionospheric behaviors over the East Asia zone during the 22 July 2009 solar eclipse. *Journal of Geophysical Research*, *115*(A10). https://doi.org/10.1029/2010JA015609

Le, H., Liu, L., Ren, Z., Chen, Y., & Zhang, H. (2020). Effects of the 21 June 2020 solar eclipse on conjugate hemispheres: A modelling study. *Journal of Geophysical Research: Space Physics*, *125*(11), e2020JA028344. https://doi.org/10.1029/2020JA028344

Le, H., Liu, L., Yue, X., & Wan, W. (2008a). The midlatitude F2 layer during solar eclipses: Observations and modelling. *Journal of Geophysical Research*, *113*(A8). https://doi.org/10.1029/2007JA013012

Le, H., Liu, L., Yue, X., & Wan, W. (2008b). The ionospheric responses to the 11 August 1999 solar eclipse: Observations and modelling. *Annales geophysicae, annales geophysicae* (Vol. 26(1), 107–116). Copernicus Publications. https://doi.org/10.5194/angeo-26-107-2008

Le, H., Liu, L., Yue, X., & Wan, W. (2009). The ionospheric behavior in conjugate hemispheres during the 3 October 2005 solar eclipse. *Annales geophysicae, annales geophysicae* (Vol. 27(1), 179–184). Copernicus Publications. https://doi.org/10.5194/angeo-27-179-2009

Le, H., Liu, L., Yue, X., Wan, W., & Ning, B. (2009). Latitudinal dependence of the ionospheric response to solar eclipses. *Journal of Geophysical Research*, *114*(A7), A07308. https://doi.org/10.1029/2009JA014072

Lei, J., Dang, T., Wang, W., Burns, A., Zhang, B., & Le, H. (2018). Long-lasting response of the global thermosphere and ionosphere to the 21 August 2017 solar eclipse. *Journal of Geophysical Research: Space Physics*, *123*(5), 4309–4316. https://doi.org/10.1029/2018JA025460

Liu, L. B., Wan, W. X., Tu, J. N., & Bao, Z. T. (2000). Modeling of the ionospheric response to the solar eclipse of 24 October 1995. *Terrestrial, Atmospheric and Oceanic Sciences*, *11*(2), 543. https://doi.org/10.3319/tao.2000.11.2.543(a)

MacPherson, B., Gonzalez, S., Sulzer, M., Bailey, G., Djuth, F., & Rodriguez, P. (2000). Measurements of the topside ionosphere over Arecibo during the total solar eclipse of February 26, 1998. *Journal of Geophysical Research*, *105*(A10), 23055–23067. https://doi.org/10.1029/2000JA000145

Madhav Haridas, M. K., & Manju, G. (2012). On the response of the ionospheric F region over Indian low-latitude station Gadanki to the annular solar eclipse of 15 January 2010. *Journal of Geophysical Research*, *117*(A1). https://doi.org/10.1029/2011JA016695

Mannucci, A. J., Wilson, B. D., & Edwards, C. D. (1993). A new method for monitoring the Earth's ionospheric total electron content using the GPS global network. In *Proceedings of the 6th international technical meeting of the satellite division of the Institute of navigation (ION GPS 1993)* (pp. 1323–1332).

Müller-Wodarg, I. C. F., Aylward, A. D., & Lockwood, M. (1998). Effects of a mid-latitude solar eclipse on the thermosphere and ionosphere-A modelling study. *Geophysical Research Letters*, *25*(20), 3787–3790. https://doi.org/10.1029/1998GL900045

Nakashima, Y., Heki, K., Takeoa, A., Cahyadic, M. N., Aditiya, A., & Yoshizawa, K. (2015). Atmospheric resonant oscillations by the 2014 eruption of the Kelud volcano, Indonesia, observed with the ionospheric total electron contents and seismic signals. *Earth and Planetary Science Letters*, *434*, 112–116. https://doi.org/10.1016/j.epsl.2015.11.029

Ozeki, M., & Heki, K. (2010). Ionospheric holes made by ballistic missiles from North Korea detected with a Japanese dense GPS array. *Journal of Geophysical Research*, *115*(A9), A09314. https://doi.org/10.1029/2010JA015531

Panda, S. K., & Gedam, S. S. (2012). GPS derived spatial ionospheric total electron content variation over South-Indian latitudes during intense geomagnetic storms. In *Optics in atmospheric propagation and adaptive systems XV* (Vol. 8535, pp. 49–58). SPIE. https://doi.org/10.1117/12.974323

Panda, S. K., & Gedam, S. S. (2013). GPS derived ionospheric TEC response to annular solar eclipse over Indian region on 15 January 2010. In *Paper presented at 2013 IEEE international conference on space science and communication (IconSpace)* (pp. 213–218). Institute of Electrical and Electronics Engineers. https://doi.org/10.1109/IconSpace.2013.6599467

Paulino, I., Figueiredo, C. A., Rodrigues, F. S., Buriti, R. A., Wrasse, C. M., Paulino, A. R., et al. (2020). Atmospheric gravity waves observed in the nightglow following the 21 August 2017 total solar eclipse. *Geophysical Research Letters*, *47*(17), e2020GL088924. https://doi.org/10.1029/2020GL088924

Picone, J. M., Hedin, A. E., Drob, D. P., & Aikin, A. C. (2002). NRLMSISE-00 empirical model of the atmosphere: Statistical comparisons and scientific issues. *Journal of Geophysical Research*, *107*(A12), SIA–15. https://doi.org/10.1029/2002JA009430

Pitout, F., Blelly, P. L., & Alcaydé, D. (2013). High-latitude ionospheric response to the solar eclipse of 1 August 2008: EISCAT observations and TRANSCAR simulation. *Journal of Atmospheric and Solar-Terrestrial Physics*, *105*, 336–349. https://doi.org/10.1016/j.jastp.2013.02.004

Rashid, Z. A. A., Momani, M. A., Sulaiman, S., Ali, M. A. M., Yatim, B., Fraser, G., & Sato, N. (2006). GPS ionospheric TEC measurement during the 23rd November 2003 total solar eclipse at Scott Base Antarctica. *Journal of Atmospheric and Solar-Terrestrial Physics*, *68*(11), 1219–1236. https://doi.org/10.1016/j.jastp.2006.03.006

Reinisch, B. W., Dandenault, P. B., Galkin, I. A., Hamel, R., & Richards, P. G. (2018). Investigation of the electron density variation during the 21 August 2017 solar eclipse. *Geophysical Research Letters*, *45*(3), 1253–1261. https://doi.org/10.1002/2017GL076572

Resende, L. C. A., Zhu, Y., Denardini, C. M., Chen, S. S., Chagas, R. A. J., Da Silva, L. A., & Liu, Z. (2021). A multi-instrumental and modelling analysis of the ionospheric responses to the solar eclipse of December 14, 2020, over the Brazilian region. *Annales Geophysicae Discussions*, *2021*, 1–24. https://doi.org/10.5194/angeo-40-191-2022

Richmond, A. D. (1995). Ionospheric electrodynamics using magnetic apex coordinates. *Journal of Geomagnetism and Geoelectricity*, *47*(2), 191–212. https://doi.org/10.5636/jgg.47.191

Rishbeth, H., & Garriott, O. K. (1969). *Introduction to ionospheric physics*. Introduction to ionospheric physics.

Salah, J. E., Oliver, W. L., Foster, J. C., Holt, J. M., Emery, B. A., & Roble, R. G. (1986). Observations of the May 30, 1984, annular solar eclipse at millstone hill. *Journal of Geophysical Research*, *91*(A2), 1651–1660. https://doi.org/10.1029/JA091iA02p01651

Schunk, R., & Nagy, A. (2009). *Ionospheres: Physics, plasma physics, and chemistry* (2nd ed.). Cambridge University Press.

Seemala, G. K., & Valladares, C. E. (2011). Statistics of total electron content depletions observed over the South American continent for the year 2008. *Radio Science*, *46*(5), RS5019. https://doi.org/10.1029/2011RS004722

Senapati, B., Huba, J. D., Kundu, B., Gahalaut, V. K., Panda, D., Mondal, S. K., & Catherine, J. K. (2020). Change in total electron content during the 26 December 2019 solar eclipse: Constraints from GNSS observations and comparison with SAMI3 model results. *Journal of Geophysical Research: Space Physics*, *125*(10), e2020JA028230. https://doi.org/10.1029/2020JA028230

Singh, A. K., Singh, R., Veenadhari, B., & Singh, A. K. (2012). Response of low latitude D-region ionosphere to the total solar eclipse of 22 July 2009 deduced from ELF/VLF analysis. *Advances in Space Research*, *50*(10), 1352–1361. https://doi.org/10.1016/j.asr.2012.07.005

Sridharan, R., Devasia, C. V., Jyoti, N., Tiwari, D., Viswanathan, K. S., & Subbarao, K. S. V. (2002). Effects of solar eclipse on the electrodynamical processes of the equatorial ionosphere: A case study during 11 August 1999 dusk time total solar eclipse over India. *Annales geophysicae, annales geophysicae* (Vol. 20(12) 1977–1985). Copernicus GmbH. https://doi.org/10.5194/angeo-20-1977-2002

Stankov, S. M., Bergeot, N., Berghmans, D., Bolsée, D., Bruyninx, C., Chevalier, J. M., et al. (2017). Multi-instrument observations of the solar eclipse on 20 March 2015 and its effects on the ionosphere over Belgium and Europe. *Journal of Space Weather and Space Climate*, *7*, A19. https://doi.org/10.1051/swsc/2017017

Strahler, A. N. (1963). *The earth sciences* (Vol. 142, pp. 1287–1288). Harper and Row. Science. https://doi.org/10.1126/science.142.3597.1287-a

Sun, Y. Y., Chen, C. H., Su, X., Wang, J., Yu, T., Xu, H. R., & Liu, J. Y. (2023). Occurrence of nighttime irregularities and their scale evolution in the ionosphere due to the solar eclipse over East Asia on 21 June 2020. *Journal of Geophysical Research: Space Physics*, *128*(2), e2022JA030936. https://doi.org/10.1029/2022JA030936

Swisdak, M., Huba, J. D., Joyce, G., & Huang, C. S. (2006). Simulation study of a positive ionospheric storm phase observed at Millstone Hill. *Geophysical Research Letters*, *33*(2). https://doi.org/10.1029/2005GL024973

Tsai, H. F., & Liu, J. Y. (1999). Ionospheric total electron content response to solar eclipses. *Journal of Geophysical Research*, *104*(A6), 12657–12668. https://doi.org/10.1029/1999JA900001

Valdés-Abreu, J. C., Díaz, M. A., Bravo, M., Báez, J. C., & Stable-Sánchez, Y. (2022). Ionospheric behavior during the 10 June 2021 annular solar eclipse and its impact on GNSS precise point positioning. *Remote Sensing*, *14*(13), 3119. https://doi.org/10.3390/rs14133119

Verhulst, T. G., & Stankov, S. M. (2020). Height dependency of solar eclipse effects: The ionospheric perspective. *Journal of Geophysical Research: Space Physics*, *125*(7), e2020JA028088. https://doi.org/10.1029/2020JA028088

Vyas, B. M., & Sunda, S. (2012). The solar eclipse and its associated ionospheric TEC variations over Indian stations on January 15, 2010. *Advances in Space Research*, *49*(3), 546–555. https://doi.org/10.1016/j.asr.2011.11.009

Wang, W., Dang, T., Lei, J., Zhang, S., Zhang, B., & Burns, A. (2019). Physical processes driving the response of the F2 region ionosphere to the 21 August 2017 solar eclipse at Millstone Hill. *Journal of Geophysical Research: Space Physics*, *124*(4), 2978–2991. https://doi.org/10.1029/2018JA025479

Wu, C., Ridley, A. J., Goncharenko, L., & Chen, G. (2018). GITM-data comparisons of the depletion and enhancement during the 2017 solar eclipse. *Geophysical Research Letters*, *45*(8), 3319–3327. https://doi.org/10.1002/2018GL077409

Zhang, S. R., Erickson, P. J., Goncharenko, L. P., Coster, A. J., Rideout, W., & Vierinen, J. (2017). Ionospheric bow waves and perturbations induced by the 21 August 2017 solar eclipse. *Geophysical Research Letters*, *44*(24), 12–067. https://doi.org/10.1002/2017GL076054

Zhang, M. L., Liu, L., & Li, Q. (2021). Modeling the global ionospheric electron densities based on the EOF decomposition of the ionospheric radio occultation observation. *Advances in Space Research*, *68*(5), 2218–2232. https://doi.org/10.1016/j.asr.2020.09.033

Zhang, S. R., Erickson, P. J., Vierinen, J., Aa, E., Rideout, W., Coster, A. J., & Goncharenko, L. P. (2021). Conjugate ionospheric perturbation during the 2017 solar eclipse. *Journal of Geophysical Research: Space Physics*, *126*(2), e2020JA028531. https://doi.org/10.1029/2020JA028531